Geothermics 111 (2023) 102716

Contents lists available at ScienceDirect

Geothermics

journal homepage: www.elsevier.com/locate/geothermics

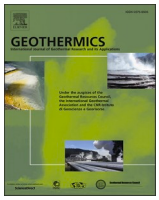

Remote exploration and monitoring of geothermal sources: A novel method for foliar element mapping using hyperspectral (VNIR-SWIR) remote sensing

Cecilia Rodriguez-Gomez [a,*], Gabor Kereszturi [a], Paramsothy Jeyakumar [a], Reddy Pullanagari [b], Robert Reeves [c], Andrew Rae [c], Jonathan N. Procter [a]

[a] School of Agriculture and Environment, Massey University, Palmerston North, New Zealand
[b] MAF digital Lab, School of Food and Advanced Technology, Massey University, Palmerston North, New Zealand
[c] GNS Science, Wairakei Research Centre, Taupo, New Zealand

ARTICLE INFO

Keywords:
Geothermal
Hyperspectral
Foliar element mapping
Random forest
Partial least squares regression
Image classification
LiDAR

ABSTRACT

Hyperspectral remote sensing is an emerging technique to develop new cost- and time-effective geophysical mapping methods. To overcome challenges introduced by plant cover in geothermal systems globally, we hypothesise that foliage can be used as a proxy to map underlying surface geothermal activity and heat-flux due to their capability on elemental uptake from geothermal fluids and host rock/soil. This study shows for the first time that foliar elemental mapping can be used to image geothermal systems using both high-resolution airborne and satellite hyperspectral images.

This study has specifically targeted kanuka shrub (*kunzea ericoides* var. *microflora*) as a proxy media to develop air- and spaceborne hyperspectral solutions to monitor inaccessible, biologically and culturally sensitive geothermal areas. Using high resolution airborne AisaFENIX and PRISMA hyperspectral data, foliar element maps for Ag, As, Ba and Sb have been developed using Kernel Partial Least Squares Regression and Random Forest classification models to track their foliar distribution and develop a conceptual model for metal and thermal induced changes in plants. Our study shows evidence that the created foliar element maps are in concordance with independent LiDAR-retrieved canopy structure and height as well as temperature effects of the underlying geothermal field. This study has proven air- and spaceborne hyperspectral sensors can indeed capture critical information within the VNIR and SWIR regions (e.g. ~452, ~500, ~670, ~820, ~970, ~1180, ~1400 and ~2000 nm) that can be used to identify metal and thermal-induced spectral changes in plants reliably (overall accuracy of 0.41–0.66) with remotely sensed imagery. Our non-invasive method using hyperspectral remote sensing can complement existing practices for exploration and management of renewable geothermal resources through timely monitoring from air- and spaceborne platforms.

1. Introduction

Visible near infrared (350–1300 nm, VNIR) and Shortwave Infrared (1300–2500 nm, SWIR) hyperspectral remote sensing has been underutilized for monitoring geothermal resources globally. This is in part due to the economic burden hyperspectral (VNIR/SWIR) imagery acquisition has represented this far, and largely due to the obstacle imposed by dense plant cover at geothermal systems, which can hamper exploration by covering hydrothermal alteration patterns and geothermal surface features (e.g. warm ground, hot springs, silica sinter) (Mia et al., 2012; Rodriguez-Gomez et al., 2021). However, plant foliage can also reflect geothermal activity by responding to the local soil and water chemistry, nutrient availability, geothermal heat and gas emissions (Mia et al., 2012; Van Manen and Reeves, 2012). Plant spectral responses to the geothermal environment have been seldomly studied, presenting an opportunity to probe into geothermal systems by remotely characterising the vegetation in the area in a novel manner. This can further improve our conceptual understanding of plant-geothermal interactions and their role in geothermal exploration.

Plants can be subject to stress due to various extreme conditions,

* Corresponding author.
E-mail addresses: c.gomez@massey.ac.nz, cecilia@eneryou.org (C. Rodriguez-Gomez).

https://doi.org/10.1016/j.geothermics.2023.102716
Received 17 October 2022; Received in revised form 20 March 2023; Accepted 29 March 2023
Available online 4 April 2023

such as high temperatures, acidic and nutrient-depleted soils, elevated amounts of elements (e.g. silver - Ag, arsenic - As, antimony - Sb) and water stress (Pippucci et al., 2015). For instance, high concentrations of antimony, sulphur, arsenic and cadmium have caused changes in spectral properties of plant canopy (e.g. red-edge shifting towards the blue due to decreasing chlorophyll contents (Manzo et al., 2013; Rathod et al., 2018)), however, these relationships have mostly been proven only in controlled experiments (i.e. pot experiments). Elements such as Ag, As and Sb are related to the deep "parental" waters in geothermal areas (Wilson et al., 2012; Simmons et al., 2016), while other elements such as barium, are correlated to the mixing of groundwater with thermal waters (Dunn, 2007), and so their location is relevant in geothermal exploration. Theoretically, vegetation can offer new insights into shallow subsurface processes via fingerprinting element concentrations and their response to metals and metalloid in geothermal areas.

Waiotapu Geothermal Field, located in the Taupo Volcanic Zone (TVZ), New Zealand, has been well studied (Hedenquist, 1991; Giggenbach et al., 1994; Reeves and Sanders, 2019) and is an excellent test-ground to upscale the findings from such controlled laboratory experiments and develop new remote sensing monitoring methods. Waiotapu Geothermal Field has great natural variability of ground conditions (e.g. low to high soil pH and temperatures up to 90 °C), with unique thermotolerant vascular species including *kunzea ericoides* var. *microflora* (i.e. kanuka) (Van Manen and Reeves, 2012). The height of kanuka has been previously related to the near-surface soil temperature where smaller plant height indicates hotter soils (Muukkonen, 2005; Smale et al., 2018). Furthermore, it has also been previously documented to uptake and translocate non-essential elements (e.g. Ag, As, Cd, Sb) (Dunn and Christie, 2020). Approximately 90% of the areal surface at the Waiotapu Geothermal Field is covered by plants (Rodriguez-Gomez et al., 2021), with a ~10% dominated by kanuka, making this plant an ideal indicator species and proxy to link plant foliage and subsurface geothermal processes for the first time.

The research objective of this study is to develop a non-intrusive method for mapping geothermal activity in densely vegetated areas. By utilising advances in laboratory, airborne and satellite-based hyperspectral remote sensing and data analytics, we propose a new methodology by combining them with elemental composition data of kanuka foliage, rock and soil samples in a multivariate image classification framework. The resultant interpretations from the element anomaly maps derived from hyperspectral (VNIR/SWIR) data were supported by independent high-resolution airborne thermal infrared (TIR) imagery and light detection and ranging (LiDAR) data, as well as, existing geological data, to establish the causality of the mapped elemental anomalies at Waiotapu Geothermal Field, New Zealand (Figs. 1-2).

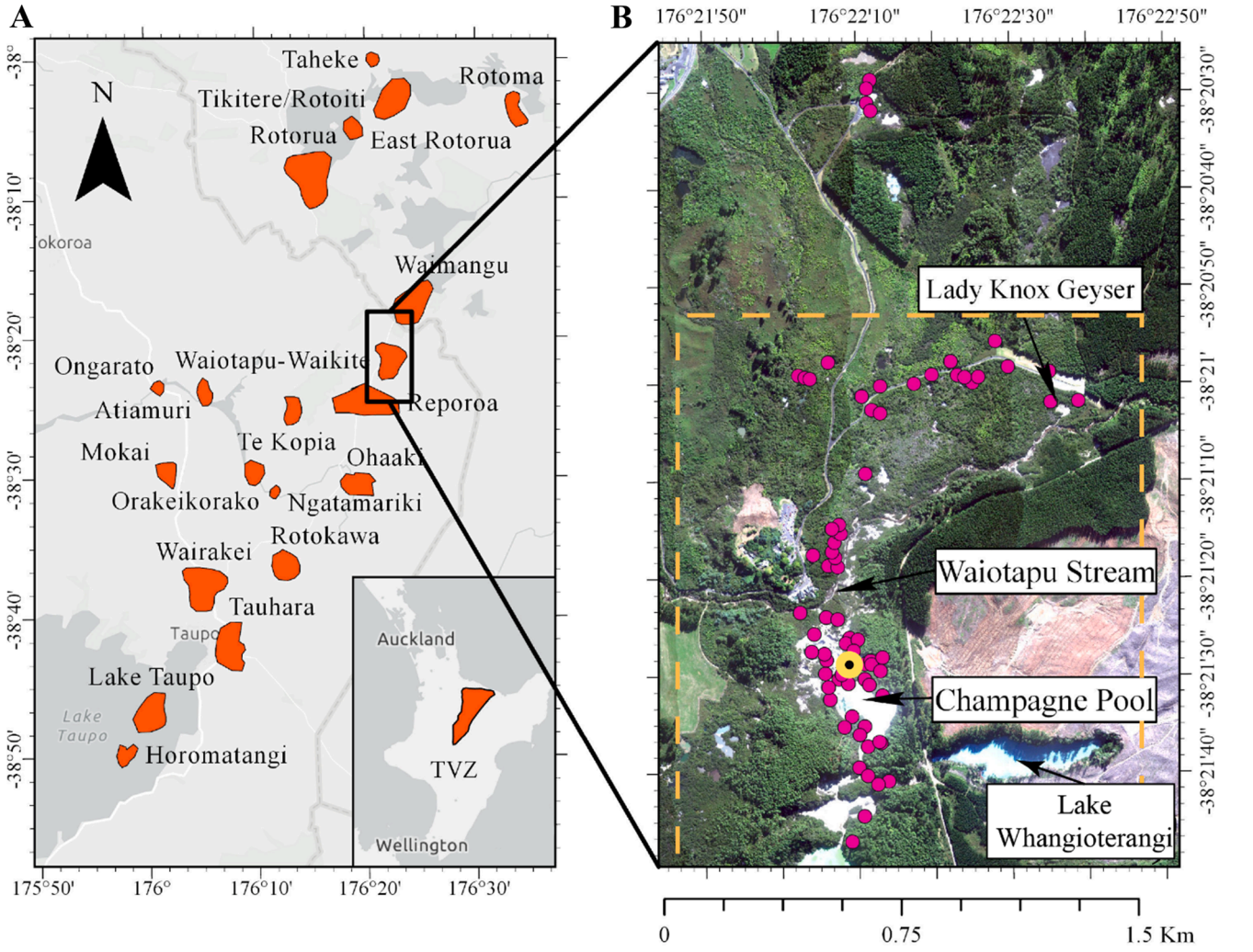

Fig. 1. (A) Location map of Waiotapu Geothermal Field within the Taupo Volcanic Zone shown with other geothermal fields [modified from Bibby et al., 1995]. (B) Central part of the Waiotapu Geothermal Field. Pink dots show the ground sampling sites. On B) the yellow dashed rectangle represents the approximate location of Figs. 6, 7 and 9. The yellow circle on B) represents the location for a rock/soil sample which had baryte mineralisation (Rodriguez-Gomez et al., 2021).

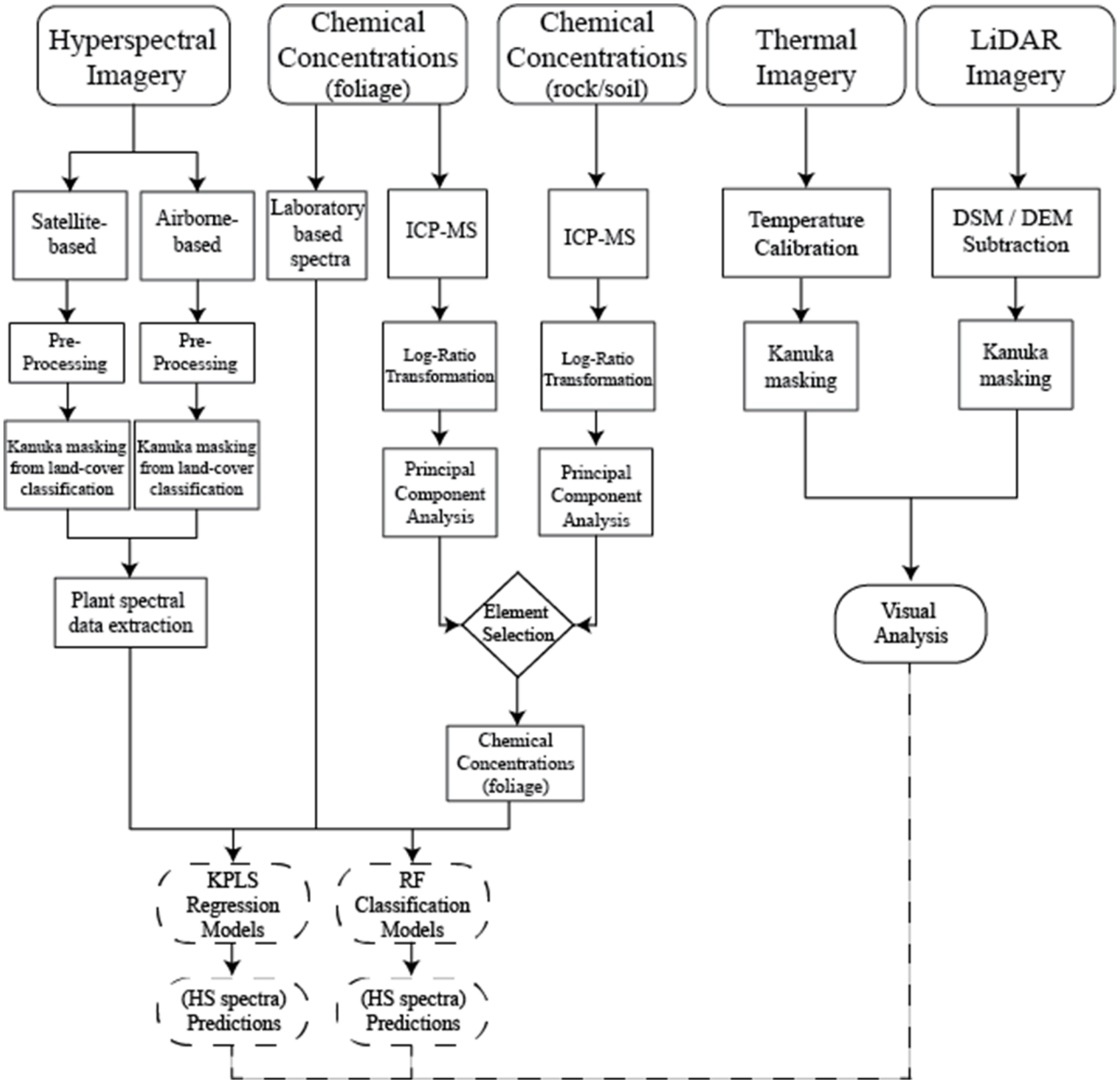

Fig. 2. The applied processing and analytical workflow of the present study. Shown in the first row is the employed data, which includes 3 types of hyperspectral (VNIR/SWIR) data (laboratory, airborne and satellite-based), along with sample's elemental concentrations to generate distribution maps interpreted in the lights of independent LiDAR and TIR imagery.

2. Study area

Waiotapu Geothermal Field forms part of the Taupo Volcanic Zone (TVZ), located in the North Island of New Zealand (Fig. 1). Geothermal activity within the TVZ is associated with the subduction of the Pacific plate under the Australian plate (Hunt et al., 1994; Wilson et al., 1995; Kissling and Weir, 2005), subject to active extension in the overriding plate (Rowland and Sibson, 2004; Seebeck et al., 2014). The TVZ basement comprises indurated sedimentary rocks referred to as 'greywacke' (Milicich et al., 2020), overlain by a sequence of pyroclastic deposits, lavas and lacustrine sedimentary rocks (Steiner, 1963; Grindley et al., 1994). Many geothermal areas in the TVZ are formed by convective hydrothermal systems with a heated reservoir at depth (1–4 km) reaching temperatures above 200 °C (Hedenquist, 1991; Kaya et al., 2014). The hot fluids interact with the host rock and groundwater, forming acid-sulphate, near-neutral high chloride and bicarbonate springs on the surface, exposing information about the subsurface activity (Pirajno, 2009).

Waiotapu Geothermal Field is one of the largest by surface features exposure of about 20 active geothermal areas in the TVZ (Fig. 1A), with a surface area of ~18 km^2 and heat flow of ~500 MWt (Bibby et al., 1995; Kaya et al., 2015). Seven wells drilled at Waiotapu Geothermal Field between 1957 and 1962 presented maximum temperatures of 195 °C with maximum depths of 1000 m (Giggenbach et al., 1994). Waiotapu is hosted by pyroclastic flows and lacustrine sediments (Lloyd, 1959; Wood, 1994; Kaya et al., 2014), presenting surface features which include fumaroles, steaming ground, hydrothermal eruption craters, mud pools, hot chloride pools, acid-sulphate altered areas, silica and sinter deposits (Grange, 1937; Lloyd, 1959; Hedenquist and Browne, 1989; Hunt et al., 1994). Hot springs and explosion craters generally follow a NE-SW trend (Hedenquist and Henley, 1985; Mongillo, 1994) with the Ngapouri and Paeroa faults as the closest active

mapped faults, located 1.5 km and 5 km to the northwest respectively (Nairn et al., 1994; Rowland and Simmons, 2012; Wood, 1994). Fluid from ~1 km depth is transported through faulting and associated fractures, offering vertical and horizontal permeability, allowing fluids to move south and west from the heat source (Hedenquist, 1982; Mongillo, 1994; Hadfield et al., 2001; Kaya et al., 2015). The thermal area drains into the Waiotapu Stream (Fig. 1B), which joins the Waikato River to the south (Lloyd, 1959).

The extreme ground conditions (e.g. acidic soils, high temperatures) present at many geothermal areas of the TVZ can host rare communities of plant species that have adapted to these conditions. These geothermal ecosystems in the TVZ include a combination of ferns (e.g. *Hypolepis* species), moss species (e.g. *Campylopus pyriformis*), liverworts (e.g. *Chiloscyphus semiteres*) and shrubs (Given, 1980; Van Manen and Reeves, 2012; Smale et al., 2018). These species can live in extremely acidic soils, in proximity to steam, with nutrient excess or deficiency, water and/or soil with high contents of heavy metals and metalloids (Given, 1980; Burns and Leathwick, 1995; Boothroyd, 2009). *Kunzea ericoides* var. *microflora* (i.e. kanuka) is a thermotolerant vascular species endemic to geothermal areas of New Zealand that can live with soil temperatures above 40 °C (Burns, 1997; Van Manen and Reeves, 2012). The height of kanuka is generally related to the near-surface soil temperature with smaller plants in hotter soils (Burns, 1997; Muukkonen, 2005; Smale et al., 2018) and has also been documented to uptake and translocate non-essential elements (e.g. Ag, As, Cd and Sb) (Dunn and Christie, 2020).

Approximately 90% of the areal surface at the Waiotapu Geothermal Field is covered by plants (Rodriguez-Gomez et al., 2021), with a ~10% dominated by kanuka. The high abundance of kanuka within geothermal systems makes this plant an ideal indicator species and proxy to link plant foliage and subsurface geothermal processes.

3. Materials and methods

3.1. Airborne and satellite hyperspectral data collection and instrumentation

An AisaFENIX sensor was used to capture an airborne hyperspectral (VNIR/SWIR) image (Table 1 and Fig. 2) between 11:20 to 12:59 NZ Standard Time on 13 April 2019. From the raw data digital numbers were converted to at-sensor radiances with CaliGeoPro (Pullanagari et al., 2016). Radiance values were converted to reflectance values using Airborne Atmospheric and Topographic Correction Model, ATCOR (Richter, 1998), using a "flat terrain" mode with image-derived water vapour column 1 g/cm using bands at 1130 nm, initial visibility of 50 km, and rural aerosol model. Followed by corrections of geometric inconsistencies performed in PARGE (Parametric Geocoding Software), with the use of ortho-photos acquired during the same flight with a Nikon D810 digital single-lens reflex camera (Schläpfer and Richter, 2002). A Savitzky-Golay (Savitzky and Golay, 1964) neighbourhood filter with a third-order polynomial smoothing (4 bands on each side) was applied to reduce noise caused by the sensor and atmospheric interferences.

Table 1
Input data characteristics at different acquisition scales. Abbreviation: FWHM – Full-width half maximum.

Scale	Laboratory-based (ASD FieldSpec)	Airborne-based (AisaFENIX)	Satellite-based (PRISMA)
Spatial Resolution (metre)	0.01	1	30
Number of Bands	2151	448	230
Spectral Sampling Interval (nm)	1.4/1.1 (VNIR/SWIR)	3.3/5.7 (VNIR/SWIR)	12
FWHM (nm)	1.4/2 (VNIR/SWIR)	3.2/12.2 (VNIR/SWIR)	12

The PRISMA (PRecursore IperSpettrale della Missione Applicativa) hyperspectral satellite provides VNIR-SWIR imagery (see Table 1 for instrument specifications) (Cogliati et al., 2021). One PRISMA tile (PRS_L2D_STD_20,200,304,222,315 _20,200,304,222,319_0001) was acquired on the 4th of March 2020 with L2D processing (i.e. geolocation, geocoded at surface reflectance, aerosol, water vapour map and cloud characterisation) was used. Figure S1 exemplifies visually the spatial and spectral differences between the airborne and satellite datasets.

3.2. Land surface cover classification

A Random Forest algorithm was utilised using labelled training samples to separate kanuka shrub spatial coverage from the other land surface cover classes (Table S1) (Ghamisi et al., 2017). Random Forest is an ensemble classifier that produces multiple decision trees from randomly selected samples (Belgiu and Drăgu, 2016). It effectively deals with large spectral datasets (Xia et al., 2014) with high co-linearity (Belgiu and Drăgu, 2016). It has been successfully applied to map tree species (Dalponte et al., 2013; Ghosh and Joshi, 2014; Cavallaro et al., 2015), hence this method was preferred in this study. Random Forest classification implemented in EnMAP-Box (van der Linden et al., 2015) was used. The classification model was computed using 500 decision trees, gini coefficient as the impurity function and stopping criteria of 1 for minimum number of samples in a node and 0 as minimum impurity. This classification was used to retrieve the aerial extent of kanuka and used as a mask later (Figure S2).

3.3. Rock/soil and foliage analysis

A total of 74 rock/soil samples along with 77 kanuka foliage samples were collected one week after the airborne survey. The sampling was targeted to compare foliar elemental uptake from a variety of geothermal environments within Waiotapu Geothermal Field, and to provide a calibration/validation dataset. Plant samples only included foliage of kanuka shrub (*kunzea ericoides* var. *microflora*), the dominant shrub species in thermally active areas in New Zealand. At the field, 'combined' samples of multiple kanuka shrubs within a 3 × 3 m area were collected to capture underlying variability.

Foliage samples were dried for 24 to 36 h at 40 °C. The leaves were separated from the stem, ground with a coffee grinder and sieved (2 mm mesh). Rock and soil samples were dried at 16–20 °C for 2 to 3 days, and then ground and sieved (1 mm mesh).

The ground samples have been analysed with an Inductively Coupled Plasma Mass Spectrometer (ICP-MS) at Bureau Veritas Mineral Laboratories, Vancouver, Canada (Fig. 2). Obtaining concentrations higher than their detection level for 45 elements (Table S2), following the standard provided by Dunn and Christie (Dunn and Christie, 2020). The mineralogy and methods used for the rock/soil samples are presented in (Rodriguez-Gomez et al., 2021) and the lithological map retrieved from such samples is shown in Figure S3.

Reflectance between 350 and 2500 nm was collected from dried and ground samples with an ASD FieldSpec High Resolution 4 equipped with a contact probe (Fig. 2). Each spectral measurement was calibrated against a white surface reference. An average from 3 spots, measured 5 times each, was obtained to create a single spectra measurement per sample, splice corrected.

The foliar and rock/soil datasets were transformed using Log Ratio (Aitchison, 1986) to convert the ICP-MS compositional data expressed in mg/kg into a suitable sample space to be analysed using standard statistical approaches (Aitchison, 1986; Muriithi, 2015). In this study, a Principal Component Analysis (PCA) was used to explore the underlying structure within the chemical compositions for both foliar and rock/soil datasets (Fig. 4). PCA calculates eigenvectors and eigenvalues of a covariance matrix presenting differences and similarities of the data (McKinley et al., 2016; Hood et al., 2019), exposing underlying patterns

in high dimensionality data. Furthermore, Pearson-type linear correlation, was also used which can also be helpful in cross-examine multivariate datasets, revealing similarities and correlations (Waskom, 2021) (Figure S4).

3.4. Classification and regression for element zonation

The ground sample data and the hyperspectral data (VNIR/SWIR) were used to develop classification and regression frameworks for zoning element distribution within the Waiotapu Geothermal Field. The spectral data (in all scales; satellite, airborne or laboratory-based) were used here as explanatory variables (Table 1 and Fig. 2), while the chemical composition data were used as target variables. All chemical concentrations were transformed using log-ratio transformation (Aitchison, 1986) to be quasi-normally distributed before classification and regression.

Cross-validation has been suggested as one of the resampling methods with the smallest bias and mean square error (Berrar, 2019), and leave one out cross-validation can be computationally demanding, however, due to the small sample population (Molinaro et al., 2005) it was selected to train both classification and regression models. To assess the prediction overall accuracy (OA) and mean absolute error (MAE) were used for classification and regression, respectively.

For the classification, the ground sample's elemental concentrations were classified into three classes (low, medium and high) using standard deviation for each selected element (Fig. 3). Due to the lack of information regarding elemental uptake of kanuka shrub living in geothermal areas a general scheme with three classes was selected. The classification was based on the distribution ($n = 77$) of each indicator element (e.g., Ag, As, Ba, and Sb). Their distributions are normal after log-transformation, therefore, medium values correspond to "median" values of the population, while the low and high values showing the depleted and enriched areas, respectively. This is a robust way for mapping spatial associations of those indicator elements.

Two sets of classification were created (Fig. 3): half standard deviation and one standard deviation. The results for half standard deviation are presented here (Table 3 and Figs. 6-7), while, the results for one standard deviation are in the supplementary material. It is important to highlight that they both have similar spatial trends (e.g. Figs. 6-7 and Figures S5-S6). Random Forest classification algorithm was used to map element concentration classes. To tune the model parameter "mtry" (i.e. the number of variables which is randomly collected to be sampled in each split) was assigned as a sequential value from 1 to 150, with the highest overall accuracy value was taken as the optimal mtry value. While the number of trees and maximum depth parameters were kept constant, as 500 and none, respectively.

For each element's classification model, the important variables were retrieved following Hong et al. (2016). It considers two indices Mean Decrease Accuracy (MDA) and Mean Decrease Gini (MDG) extracted from the model. Utilising both indices considers not only the importance but also the impurity of the variable. These values were ranked and added to each other to compute a single total variable score and select the important wavelengths (Fig. 8). Only the highest 10% was deemed as important and plotted in comparison to the average plant spectral reflectance for laboratory, airborne and satellite based spectral signatures (Fig. 8).

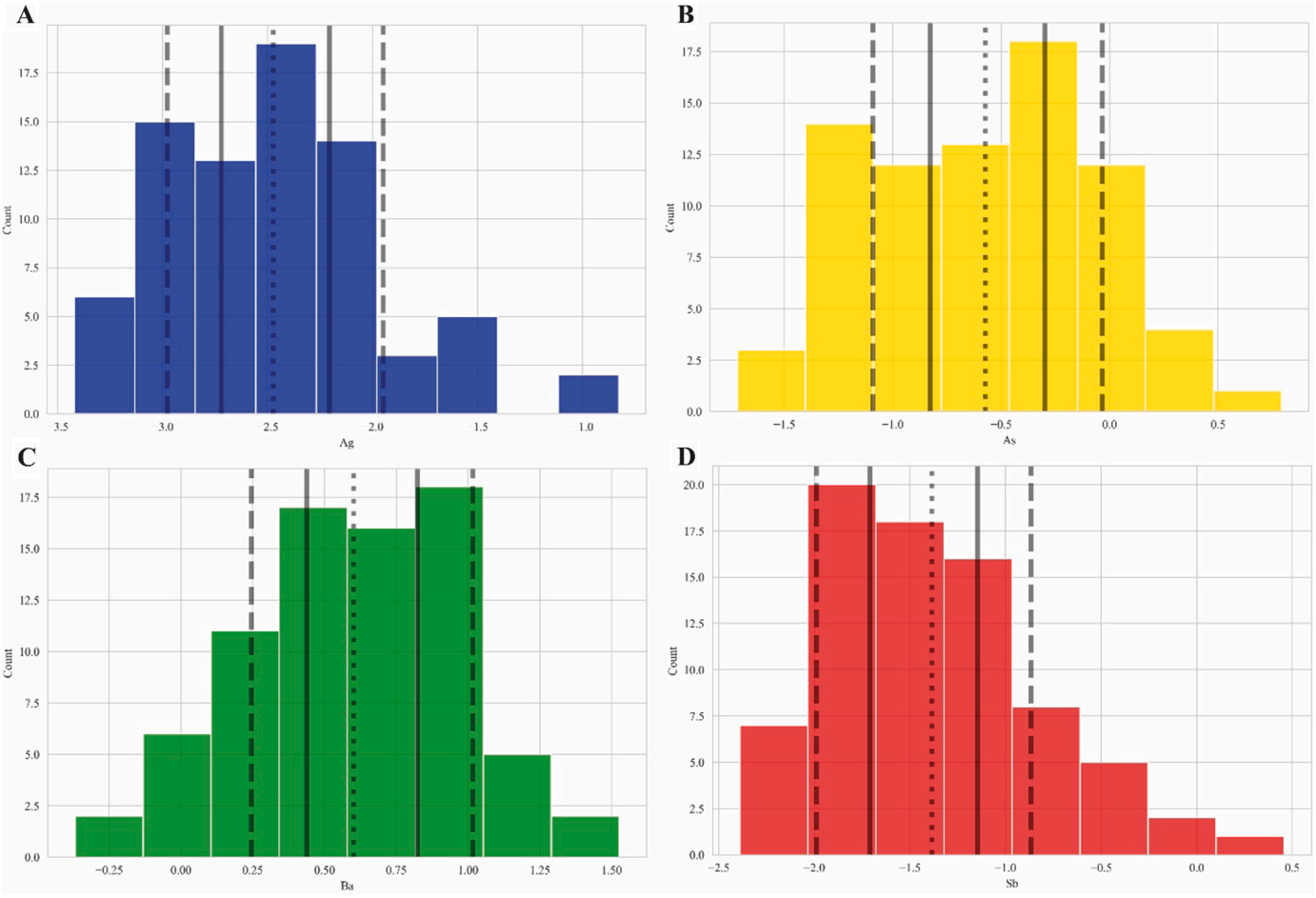

Fig. 3. Foliar chemical concentration after a log-ratio transformation showing the mean (dotted line), half- (solid line) and one-standard deviation (dashed line). (A) Silver, (B) Arsenic, (C) Barium and (D) Antimony.

For regression, Kernel Partial Least Squares (KPLS), an extension of the original Partial Least Squares multivariate statistical technique (Wold et al., 2001) was applied to the datasets (Table S3) (Figures S2-S3). KPLS transforms the original data to a high dimensional feature space using kernel functions for non-linear structure input data and linear PLS for feature extraction (Rosipal, 2003). It can be used to model relations between sets of observed variables and solve non-linear problems, which has been used for similar plant datasets before (Pullanagari et al., 2016; Chakraborty et al., 2021). The number of PLS were estimated based on the data using LOOCV, and the model with the least MAE was selected.

3.5. Thermal infrared and LiDAR data

Night-time airborne Thermal Infrared (TIR) imagery over the Waiotapu Geothermal Field was collected on 13 April 2019 with a FLIR A615 TIR camera, following Reeves & Sanders (2019). The survey flight altitude was 1–1.25 km above ground level. Resulting in a TIR image of ~0.7 m spatial resolution covering a total area of ~11 km^2. In-situ water temperatures were measured with a Yokogawa TX10 digital temperature metre which is connected to a K type thermocouple. The calibration measurements were taken at the same time as image acquisition to convert the airborne brightness values to absolute temperature (Reeves and Sanders, 2019). Because temperature values were calibrated against water bodies; temperature from other surfaces (i.e. rock/soil and foliage) with different emissivity must be used with caution as they will only be approximations (Rodriguez-Gomez et al., 2021).

The airborne LiDAR data were acquired in April 2019 and obtained from Land Information New Zealand (LINZ) Data Service as part of the Waikato – Reporoa and Upper Piako River LiDAR survey for Lincoln Agritech Limited. The survey was captured in New Zealand Transverse Mercator Projection with a spatial resolution of 1 m. The individual tiles of Digital Terrain Model (DTM) and Digital Surface Model (DSM) data were mosaicked together to form two single images, respectively, covering the area of interest. The DTM mosaic was then subtracted from the DSM model to obtain plant height.

The TIR and LiDAR datasets and their derivates provide approximate surface temperatures and plant height which have been studied previously at Waiotapu Geothermal Field (Burns, 1997; Van Manen and Reeves, 2012). Thus, they allow independent corroboration of the retrieved foliar element maps to further understand the effect of soil temperatures as well as the chemical uptake of plants growing in geothermal settings.

4. Results

4.1. Rock/Soil and foliar chemical relations

The bulk chemistry of rock/soil and foliar samples show 45 elements above the detection limit (Table S2) to which a log-ratio transformation was applied to normalize the compositional data. The PCA analysis and linear correlations showed silver (Ag), gold (Au), arsenic (As) and antimony (Sb) with similar behaviour in both rock/soil and foliar datasets, positively influencing PC1 (Fig. 4), towards the samples closer to Champagne Pool (Fig. 1). Champagne Pool in Waiotapu Geothermal Field, which name derives from the abundance of CO_2 bubbles coming to surface, is one of the largest focal points from where near-neutral high-chloride deep geothermal water discharges to the surface (Fig. 1). The upflow here is enriched in metals (e.g. Ag, Au) and metalloids (e.g. As, Sb) (Weissberg, 1969; Wilson et al., 2012; Simmons et al., 2016). Lady Knox Geyser is another area with near-neutral high-chloride waters (Fig. 1); however, the acquired field samples from this area do not show high concentrations of Au, As and/or Sb (Figures S6-S7). This can be attributed to the smaller discharge in Lady Knox Geyser compared to Champagne Pool and the sampling locations being opposite to the groundwater flow direction.

In contrast, zinc (Zn), barium (Ba), and cadmium (Cd - only from foliar samples) showed the opposite behaviour in both rock/soil and foliar (Fig. 4). The differences between rock/soil and foliar samples for Ba (large Ba concentrations in plant samples but not in rock/soil samples) visible in the PCA (Fig. 4) are attributed to the type of rock/soil samples (e.g. northern area samples have a higher organic matter content while southern areas are mostly lithology-dominated). Ba concentration in foliage shows a clear opposite trend to Ag, As and Sb (Fig. 4).

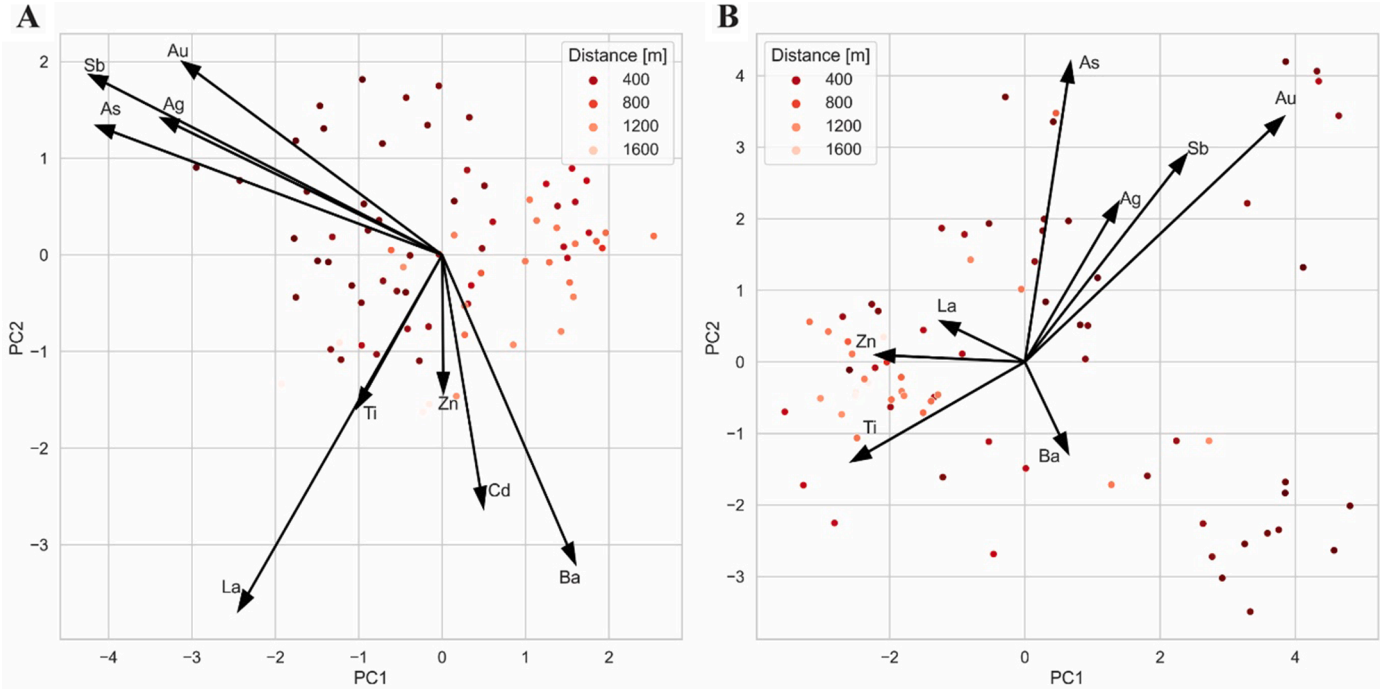

Fig. 4. Score and loading plots of the Principal Component 1 (PC1) and Principal Component 2 (PC2) for (A) the foliar samples and (B) the rock/soil samples from Waiotapu Geothermal Field. Points are colour coded based on the distance from Champagne Pool.

The opposite trend seems to be correlate with the distance from Champagne Pool (Fig. 4), with high Ba values occurring towards areas of water mixing further away from the Champagne Pool (Dunn, 2007).

The complexity of the geothermal system and furthermore, the diverse controls on the uptake of elements by plants (Shtangeeva et al., 2011; Farooq et al., 2016), is reflected in weak to moderate co-occurrence values between rock/soil and foliar chemical concentrations (Fig. 5): Ag (Pearson R: 0.28 and p-value: <0.01), As (Pearson R: 0.17 and p-value: 0.01), Ba (Pearson R: −0.38 and p-value: 0.18), and Sb (Pearson R: 0.40 and p-value: 0.18). Inter-elemental correlations with Pearson R for rock/soil and foliar chemical concentrations are shown in Figure S4. The low to moderate correlation is not unexpected, other studies have also presented that elemental concentrations between soil and plant samples do not exactly co-vary, due to chemical and biological factors, such as variations in pH and bacterial richness, as well as temperature differences (Borovička et al., 2006; Shtangeeva et al., 2011; Crowther et al., 2019; Sleimi et al., 2021; Ubeynarayana et al., 2021). Furthermore, the element uptake rates can vary amongst plant species and are dependant on their broader environment such as the soil pH (e.g. (Khan et al., 2015; Shahid et al., 2017)).

Overall rock/soil samples showed higher elemental concentrations than the foliar samples (Table 2). In this case, the bioaccumulation ratio was element-specific and non-linear, reflecting the complexity of the geothermal system and how the interrelations between rock/soil and foliar vary greatly throughout Waiotapu Geothermal Field. On average, higher bioaccumulation ratios were present in Ag and Ba, while As and Sb bioaccumulation ratios were significantly lower (Table 2). This can potentially indicate a barrier in the rhizosphere caused by mycorrhizal associations, which assist the plant obtaining nutrients and filtering toxic elements (Moyersoen and Beever, 2004). Some measured

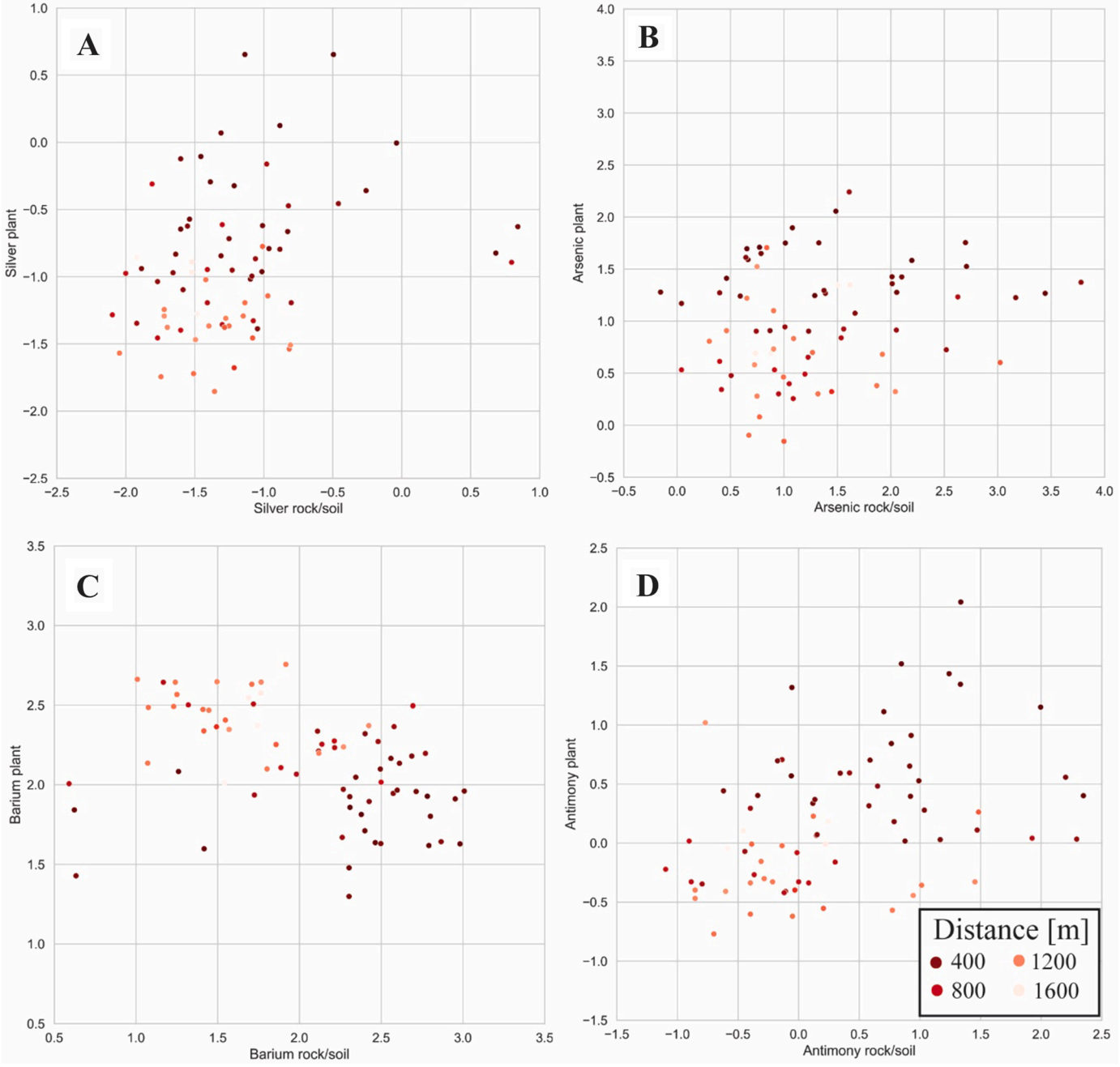

Fig. 5. Scatterplots of log-ratio transformed chemical concentrations for foliage (y-axis) against rock/soil (x-axis), colour coded by the distance from Champagne Pool in meters. (A) Silver, (B) Arsenic, (C) Barium and (D) Antimony.

Table 2
Chemical concentration ranges for rock/soil and foliar samples for silver, arsenic, barium, and antimony, phytotoxic levels for other plant species and bioaccumulation ratios from site samples.

Element	Rock/Soil [mg/kg]		Foliage [mg/kg]		Phytotoxic level [mg/kg] (other plant species)	Bioaccumulation Ratio
	Minimum	Maximum	Minimum	Maximum		Average(all samples)
Silver (Ag)	0.01	6.95	0.0003	0.15	3.8 in leaves (Wang et al., 2017)	0.15
Arsenic (As)	0.7	12,000	0.019	6.21	0.003 in leaves (Wallace et al., 1980)	0.06
Barium (Ba)	3.9	1018.3	0.42	33.65	137 in soil (Suwa et al., 2008)	0.14
Antimony (Sb)	0.02	392	0.04	2.87	0.15 in leaves (Shtangeeva et al., 2011)	0.052

elemental concentrations in foliar samples are well above the toxic level tolerated in other species (Table 2), pointing to their potential as stress factors for plant growth in geothermal environments. Spectrally the kanuka samples show differences between high concentration and low concentration samples which are most prominent in 400–1500 nm and 1700 to 2200 nm (e.g. Figure S7).

4.2. Classification and regression models

The classification on laboratory-based spectral data on the foliage samples showed overall accuracy (OA) between 0.41 and 0.47 with LOOCV without removing any outliers to keep complexity (Table 3) . The airborne-based spectral data classification showed an improved overall accuracy between 0.45 and 0.57 after LOOCV (Table 3). Satellite-based spectral data classification had an overall higher accuracy between 0.57 and 0.66 after LOOCV (Table 3). Higher OA values from the airborne- and satellite-based data are possibly caused by the hyperspectral image being partially sensitive to canopy structure information (Croft et al., 2014; Almeida et al., 2021; Zeng et al., 2022) and samples larger area due to their larger spatial resolutions. Any outliers in the training/validation datasets can significantly lower the overall accuracy when LOOCV is used (Molinaro et al., 2005; Berrar, 2019), regardless, outliers were kept as they represent the high variability in the system.

Airborne and satellite-based classification maps, showed good agreement between the observed spatial distributions of the samples, despite their large contrast in spatial resolutions (1 m versus 30 m). Classification maps for As, As and Sb indicate high concentrations near Champagne Pool, whereas Ba is enriched further away from the Champagne Pool (Figs. 6-7).

The satellite-based classification models and predictions in conjunction with the ICP-MS foliar chemical data were performed to test the upscaling capability of this method for satellite imagery (Fig. 7). The same area of kanuka coverage from the airborne-based image was employed as a mask to extract the kanuka covered pixels from the co-registration (Root Mean Square Error of 1.5 m) satellite image. The satellite-based classification models showed overall accuracy between 0.57 and 0.66, slightly higher than the airborne-based predictions (Table 3).

The performance of the regression models in laboratory and airborne-based datasets was deficient, with R^2 values between 0.02 to 0.26 and 0.17 to 0.23, respectively. Intriguingly, the maps are spatially congruent; regardless of unsatisfactory performance (e.g. see Table S4, Figure S5 and S6).

Table 3
Classification overall accuracy values for laboratory-based, airborne-based and satellite-based random forest models. Class-wise error and error matrix is included in the supplementary data.

Element	Overall Accuracy		
	Laboratory-based	Airborne-based	Satellite-based
Silver (Ag)	0.41	0.45	0.58
Arsenic (As)	0.43	0.57	0.63
Barium (Ba)	0.45	0.5	0.66
Antimony (Sb)	0.47	0.48	0.57

From the classification models of laboratory, airborne and satellite-based datasets, the MDA and MDG values from each element's model were extracted, ranked and added to compute a single total variable score and select the important wavelengths (Fig. 8), following Hong et al., 2016. Only the highest 10% was deemed as important and plotted in comparison to the average plant spectral reflectance for laboratory, airborne and satellite-based spectral signatures (Fig. 8). Most of the selected important wavelengths are in the visible range for all datasets, and >1000 nm for the laboratory-based dataset (Fig. 8).

5. Spatial distribution of canopy height and approximate surface temperatures

The elemental distribution maps generated from elemental ICP-MS measurements and hyperspectral (VNIR/SWIR) spectra (airborne and satellite) can be compared with the LiDAR-derived plant height and TIR-based approximate ground temperature maps, only within the kanuka land cover type (Fig. 9). Both datasets correlate well with geothermal activity and provide independent corroboration for the generated elemental distribution maps. The two datasets showed a trend between decreasing canopy height and increasing approximate surface temperature within a clear boundary (Fig. 9C). This observation is consistent with previous studies (Burns and Leathwick, 1995; Muukkonen, 2005; Van Manen and Reeves, 2012). The abundance of shorter plants at low temperatures is interpreted to be due to young plants that have not reached full canopy height and some misclassification of kanuka for rock/soil (~3% misclassification, error matrix in Table S1).

Furthermore, Ag, As and Sb present similar behaviour in terms of plant height (Figure S10). The areas with high elemental distribution of these three elements tend to manifest as "shorter" kanuka plants, while the low elemental distributions often co-occur with "taller" kanuka plants. On the other hand, Ba presents the opposite behaviour (Figure S10).

6. Discussion

6.1. A new tool for elemental zonation using hyperspectral remote sensing

Previous studies have reported changes in the physical and chemical behaviour of plants living in geothermal environments (Burns and Leathwick, 1995; Van Manen and Reeves, 2012; Lattanzi et al., 2020). Such physicochemical changes can become an exploration and monitoring proxy if quantified with hyperspectral imaging. For the first time, this study shows the fingerprinting of physicochemical changes in foliage due to geothermal activity, which can be captured spatially and independently by laboratory, airborne and satellite-based hyperspectral (VNIR/SWIR) remote sensing.

The predicted element zonation maps show strong similarities with the ground samples/field observations (Figs. 6-7 and Figures S11-S12). The predicted element zones mostly co-occur spatially with physical changes to the canopy structure (e.g. LiDAR-based height) and TIR-based ground temperature (Fig. 9). These changes in kanuka canopy structure are in line with ground-based studies, documenting kanuka shrub becomes significantly shorter (<0.5 m in height) when ground temperatures are >40 °C (Burns and Leathwick, 1995; Smale et al.,

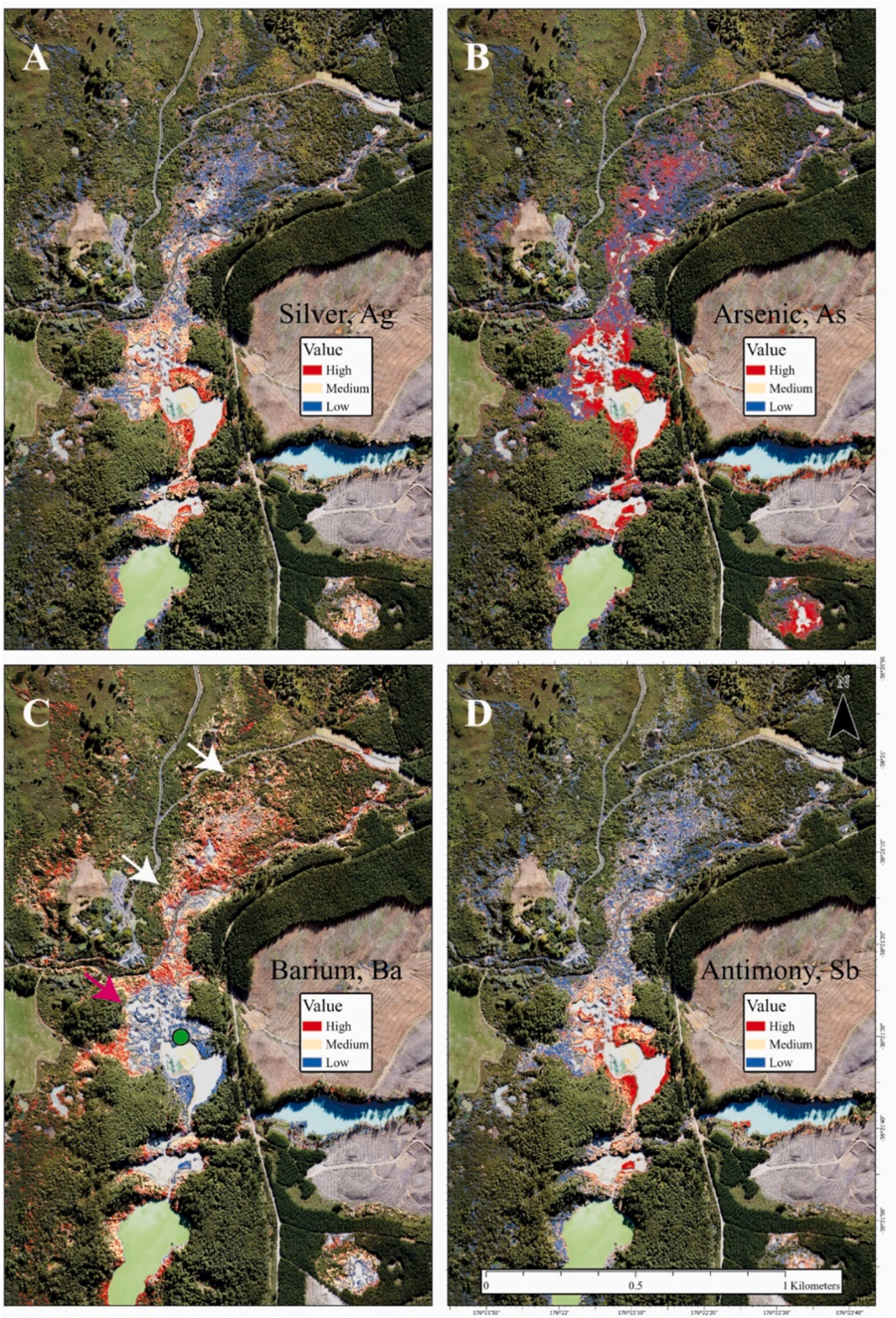

Fig. 6. Predictions for silver (A), arsenic (B), barium (C), and antimony (D) concentration in plants from airborne-based imagery (high, medium, and low). (C) White arrows point to inferred groundwater mixing and low pH. Pink arrow points to high sulphate areas where barium is not bioavailable to plants. Green circle is the location of rock/soil sample_022 which has baryte crystals (Rodriguez-Gomez et al., 2021).

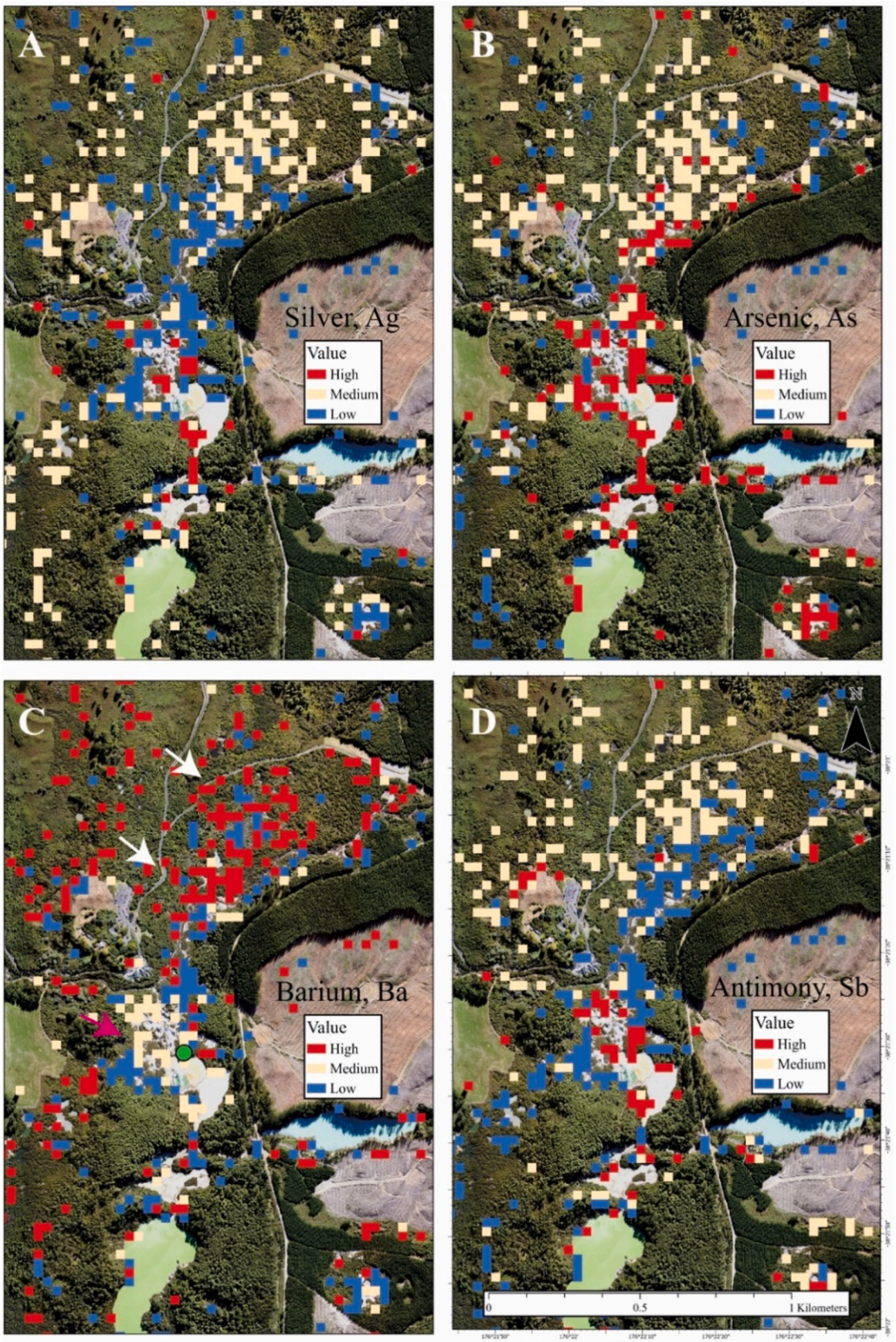

Fig. 7. Predictions for silver (A), arsenic (B), barium (C), and antimony (D) concentration in plants from satellite-based imagery (high, medium, and low). (C) White arrows point to inferred groundwater mixing and low pH. Pink arrow points to high sulphate areas where barium is not bioavailable to plants. Green circle is the location of rock/soil sample_022 which has baryte crystals (Rodriguez-Gomez et al., 2021).

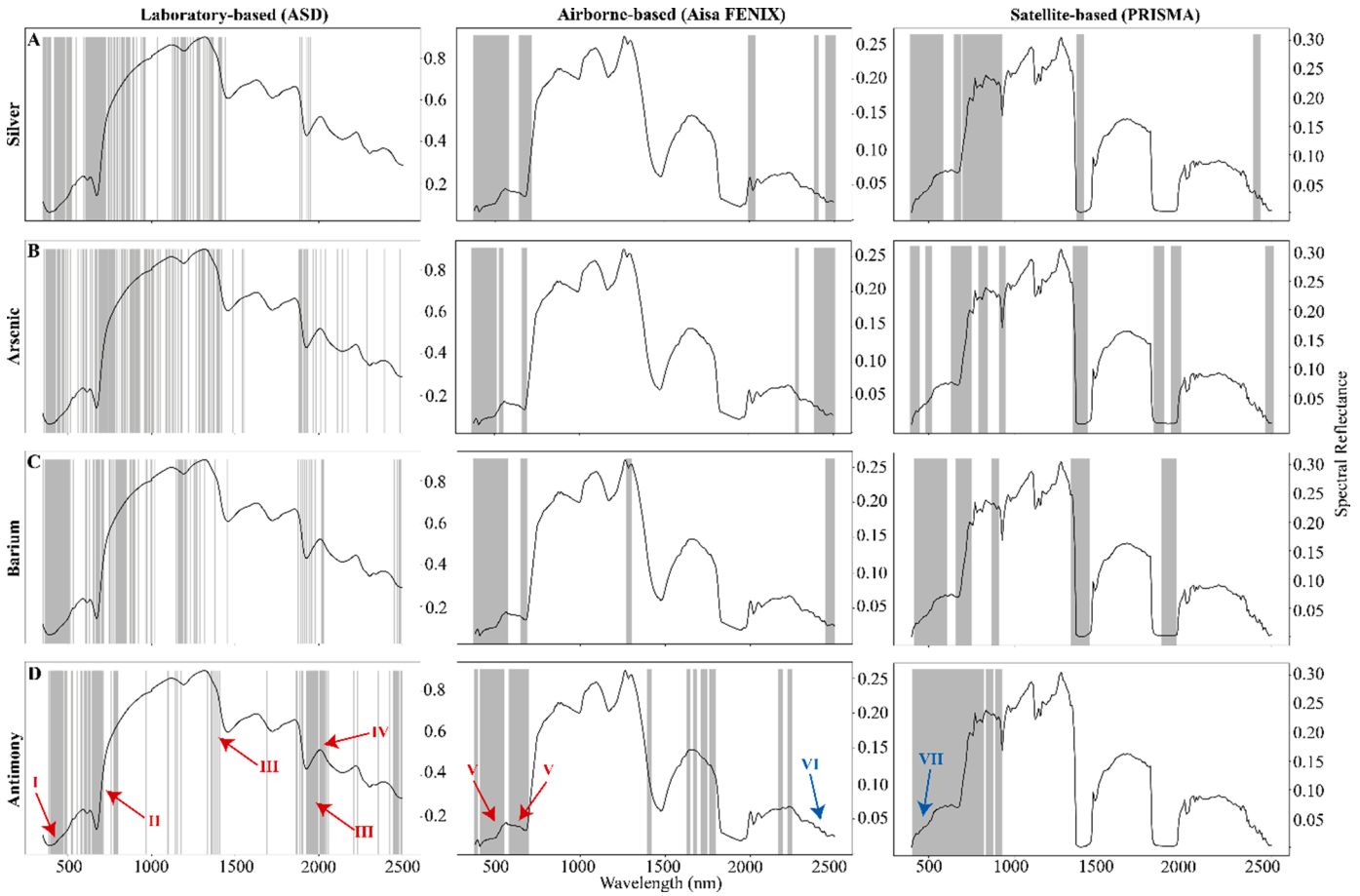

Fig. 8. Important wavelengths derived from random forest classification models, shown per element (rows) for laboratory-, airborne and satellite-based (columns). (A) Silver, (B) Arsenic, (C) Barium and (D) Antimony. The presented plant spectral reflectance shown is the average spectral reflectance from all field sample sites as measured by laboratory equipment (ASD FieldSpec), airborne (AisaFENIX) and satellite (PRISMA). Red arrows point to significant absorption features (I) chlorophyll and carotenoid-related absorption(~452 nm), (II) Red edge region (680 – 750 nm), (III) Metal-induced stress ~1370 - 1570 nm and ~1825 - 2170 nm, (IV) water content ~ 2000 nm, (V) degradation of foliar pigments 470 – 510 nm and at 550 – 750 nm. Blue arrows point to noisy regions of the spectra (VI) <400 nm and (VII) > 2450 nm.

2018), and roots start growing horizontally (Van Manen and Reeves, 2012). Spectral changes can therefore be due to a combination of leaf area and chlorophyll content changes, degradation of carotenoids, as well as reduction of plant biomass (Shtangeeva et al., 2011; Sanches et al., 2013; Dong et al., 2019). Nevertheless, high concentrations of Ag, As and Sb can also occur in canopies >1 m in height (Figure S10).

The remotely (e.g. airborne and satellite) mapped elemental anomalies alone could still indicate physical variations to the canopy structures associated with the underlying geothermal system (Figs. 6-7). However, our laboratory-based classification models returned similar overall accuracy to the airborne models (0.41–0.47 versus 0.45–0.57, Table 3), and very similar spectral band importance regions within the spectrum studied, even though the laboratory-based samples had all been dried and grounded. This highlights that the retrieved foliar element concentration represents a combined effect of thermal and metal-induced stress within an active geothermal area. The marginal but better OA for the air- and spaceborne data (e.g. Table 3) can further indicate a small contribution from the canopy structure and neighbouring objects (e.g. exposed ground) due to the increased pixel size.

6.2. *Remote detection of foliar element concentration in geothermal systems*

Regardless of being thermal-, water-, metal- or nutrient-induced, plant stress can often be detected within VNIR by multispectral (Poblete et al., 2020) and hyperspectral remote sensing (Slonecker et al., 2009; Delalieux et al., 2009; Rathod et al., 2018). The assessment of important wavelengths in remotely detected foliar element maps (Fig. 8) can further yield insights into geothermal systems and changes in shallow hydrological properties. Our study assessed Ag, As, Sb and Ba which are commonly occurring elements in geothermal systems globally (e.g. Yellowstone in U.S.A., Cerro Pabellon in Chile, The Geysers, U.S.A.) (Smith et al., 1987; Macur et al., 2004; Reich et al., 2020). While those elements alone have no unique spectral reflectance within the VNIR and SWIR regions, their presence in plants can be inferred indirectly due to the spectral changes. Our classification models returned important wavelengths for all elements, with unique important wavelengths detected for Ag, Sb and Ba, whereas As shares most of its important wavelengths with the other elements (Table S5).

Within the VNIR region, the decrease of chlorophyll-a absorption can cause shifts in the visible and red regions (Sims and Gamon, 2002; Sanches et al., 2013) (Table S2), indicating metal and thermal stress (Rathod et al., 2018). In this region, all four elements show an important wavelength at ~452 nm in the laboratory and airborne-based models (Fig. 8), which coincides with chlorophyll and carotenoid-related absorption (Sanches et al., 2013). At longer wavelengths, Ag, As and Sb for laboratory-based (~642–696 nm) and airborne-based models (~490, ~510, and ~670 nm) returned a series of important wavelengths (Table S5), located in a wavelength range that has been associated to the degradation of foliar pigments at 470–510 nm and at 550–750 nm (I.D.

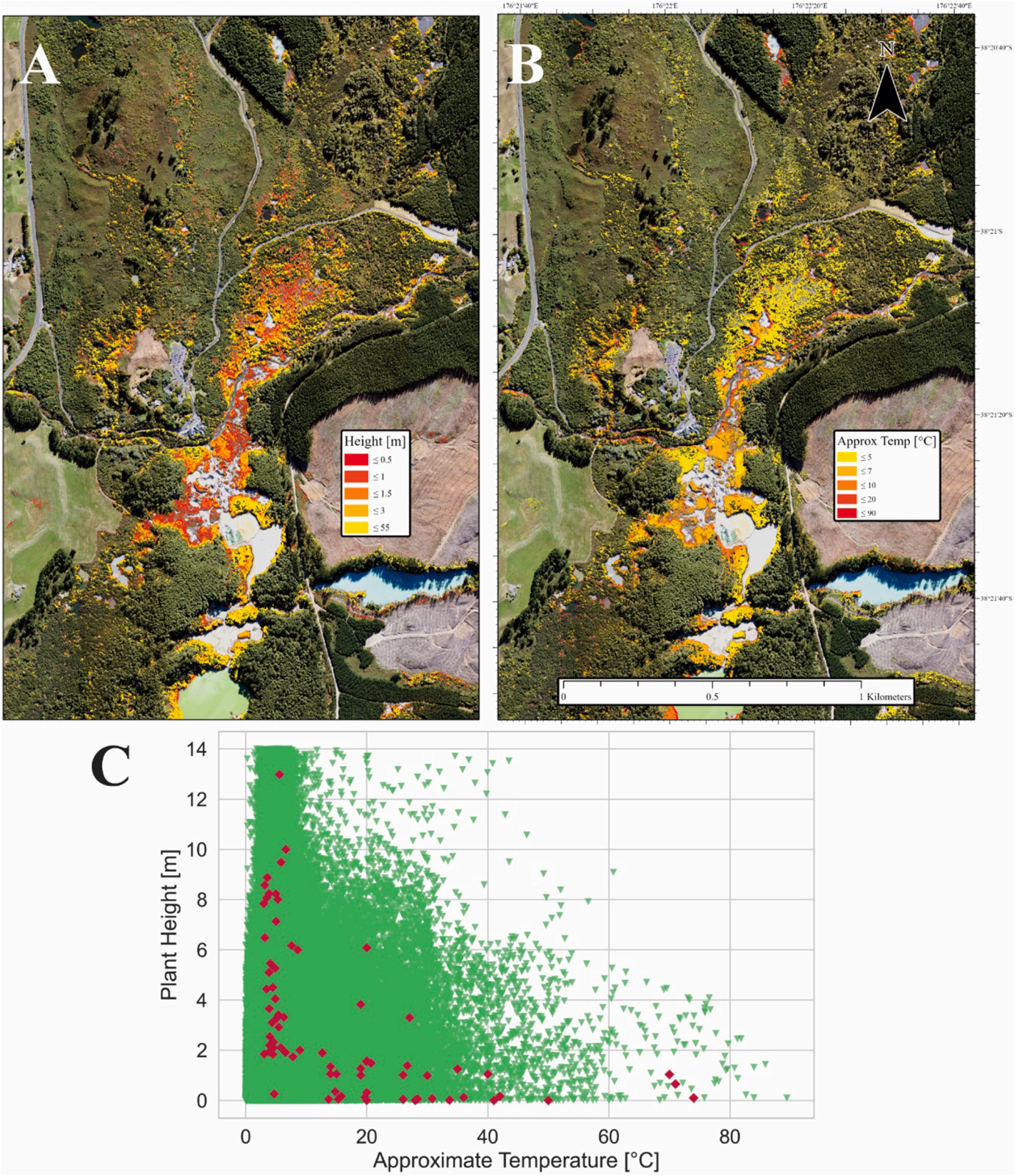

Fig. 9. (A) Kanuka plant heights from the LiDAR data. (B) Approximate temperatures from airborne-based thermal infrared data. (C) Comparison plot between plant height in meters and approximate temperatures in °C. Red diamonds show the distribution of the plant field samples.

Sanches et al., 2013) (Fig. 8). Ba also presents important wavelengths within these two regions at ~480, ~500, and ~670 nm, both in the laboratory and airborne-based models and ~500 and ~690 nm in the laboratory and satellite-based models (Table S5). Notably, the four elements present an important wavelength at ~720 nm for the satellite-based model, a wavelength where a shift in the red-edge can signal metal-induced stress (Slonecker et al., 2009). While this region coincides with a minor water vapour absorption feature (Duarte, 1995),

this part of the spectrum has also been highlighted in the laboratory-based models (Table S5).

Our foliar element classification model highlighted a range of important wavelengths between 800 and 1300 nm, indicative of internal leaf structure damage due to external environmental factors (Roy, 1989; Rathod et al., 2018). For example, Ag has been reported to inhibit water flow across cell membranes leading to leaf damage (Cox et al., 2016; Wang et al., 2018). Similar to Ag, exposure to As can damage cellular membranes, causing electrolyte leakage (Kabata-Pendias, 2010; Finnegan and Chen, 2012). Both, Ag and As share important wavelengths in the laboratory-based model at ~820–890 and ~1133 nm. Silver presents important wavelengths in the satellite-based model from ~800–910 nm, while As does at ~820 and ~930 nm. Sb can cause growth retardation and inhibition of photosynthesis (Feng et al., 2013), presenting important wavelength regions for the laboratory-based model at ~970–1180 nm, and in the satellite-based model at ~887 nm. These three elements (Ag, As, and Sb) do not present any important wavelengths in the airborne-based model in this region (Table S5).

Distinctly, Ba presents important wavelengths in the three scales, sharing wavelengths at ~820 and ~890 nm with Ag, at ~820–890 and ~1180 nm with As and ~1180 nm with Sb at the laboratory-based scale. The airborne-based model has important wavelengths at ~1280 nm and for the satellite-based model there are important wavelengths at ~802–910 nm (Table S5). Barium, which can be toxic to plants (>5 mg/kg) (Dunn, 2007; World Health Organization, 2016), can cause stomatal closure and perturbation in the foliar metabolism (Suwa et al., 2008), causing overall plant growth rate reduction (Sleimi et al., 2021). The stomata function regulates gas transfer between plants and the atmosphere for photosynthesis, plants living in geothermal areas have been reported to present lower stomatal conductance and cell membrane damage (Pippucci et al., 2015).

Within the SWIR, the leaf water content can impact spectral reflectance between ~1300–2500 nm, causing 78–83% of the reflectance (Tucker, 1979). Water absorption regions are a valuable indicator of metal-stress, at wavelengths ~1370–1570 nm and ~1825–2170 nm (Curran, 1989; Rathod et al., 2018) (Fig. 8). Some of these wavelengths are also sensitive to lignin and protein production, which can be affected by metal uptake-induced stress (Götze et al., 2010; Kokaly and Skidmore, 2015). Our foliar element maps show much less important wavelengths from the SWIR region than the VNIR (Fig. 8). This can be due to SWIR data having more noise which can degrade model performance, as well as atmospheric processes. Important wavelengths close to indicative regions at laboratory-based scale for Ag and As are located at ~1400, ~1880, and ~2100 nm and several at ~2000 nm for satellite-based models. Ag and Sb share important wavelengths at laboratory-based scale at ~1940, nm, whereas, As and Sb only at ~1980 nm and for satellite-based models at ~ 1400 nm. The presence of important wavelengths in this range throughout the three scales indicates deterioration of the foliar health regarding water content.

The high amount of shared important wavelengths by Ag, As and Sb reflect their similar behaviour in the geothermal environment, congruent with the PCA results (Fig. 4), as their solubility and toxicities strongly depend on pH and temperature (Ballantyne and Moore, 1988; Wilson et al., 2010). These factors directly affect kanuka's foliar uptake regardless of the possible mycorrhizal associations which assist kanuka in obtaining nutrients and filtering the uptake of toxic elements (Moyersoen and Beever, 2004), seemingly affecting the plant similarly. In contrast, Ba presents a different behaviour which shows up in its important wavelengths, highlighting its slightly different effects in the foliar internal structure. Furthermore, Ba also has recurrent important wavelengths in the range from ~1280–1400 nm for the three scales (Fig. 8) (Table S5), where leaf internal damage and foliar water content are detected (Rathod et al., 2018).

The classification error metrics resulted in moderate results (0.41 to 0.66), in future studies other pre-processing and post-processing techniques should be tested (e.g. adjusting atmospheric values, pixel unmixing, and elemental data transformations). Furthermore acquiring higher number of samples can allow for different validation methods to be tested (e.g. K-fold cross validation, bootstrapping). Regardless of the moderate error metrics results, the agreement between laboratory, airborne and satellite-based important wavelength areas and their relation to such wavelengths to vital plant processes, as well as their spatial congruency, highlights the feasibility of remote sensing to study the behaviour of plants living in geothermal areas.

6.3. Geology and biogeochemistry - relations and processes

Waiotapu Geothermal Field is an ignimbrite-hosted geothermal system with inherent complexity due to permeability and porosity changes influencing groundwater movement and hydrothermal alteration at cm to metre scales. Overall, the northern area is characterised by acid-sulphate alteration, whereas the southern region has near-neutral high-chloride water pools with silica deposits (Giggenbach et al., 1994; Rodriguez-Gomez et al., 2021), these surface features are tightly intermixed in some areas (Figure S2).

Both ground samples and foliar maps show elevated Ag, As and Sb concentrations in proximity to Champagne Pool (Fig. 2), indicating the current location of the deep-seated, chloride-rich and near-neutral pH water discharge. These elements signal deep parental waters (Bundschuh and Maity, 2015), and epithermal ore deposits (Simmons et al., 2016; Smith et al., 1987). Elements like As and Sb, when in soluble state and under certain pH and temperature conditions (Ballantyne and Moore, 1988; Tschan et al., 2009; Wilson et al., 2010) become readily bioavailable and are extremely toxic to plants (Finnegan and Chen, 2012). Mycorrhizal associations can assist plants by filtrating the translocation of toxic elements from the root (e.g. As and Sb) and obtaining nutrients for the plant, in exchange for glucose and energy attached to the roots (Dunn, 2007; Li et al., 2018; Tschan et al., 2009). But as shown by our samples, a considerable and toxic amount of these elements gets translocated to the foliage of kanuka (Table 2), affecting the foliage to a degree detectable by hyperspectral remote sensing (VNIR/SWIR).

Further away from the high-chloride, near-neutral pH water pools, Ag, As and Sb decrease in concentration, while other elements, such as Ba become bioavailable and easily uptaken by plants. Foliar enrichment in Ba is a good pathfinder element to identify zones where hot geothermal water is mixing with cold groundwater in the periphery of epithermal systems (Bundschuh and Maity, 2015; Dunn, 2007). Ba solubility increases with decreasing pH, whilst in waters with high sulphate content, Ba reacts to form an insoluble salt (World Health Organization, 2016). We observe this behaviour within our data and classification maps as Ba foliar concentrations increase in the peripheral areas (white arrows in Figs. 6-7) and decrease in areas with neutral-pH fluids with high concentrations of sulphate where Ba is not bioavailable to plants (pink arrow in Figs. 6-7). This is also observable between rock/soil and foliar Ba concentrations (Figures S6-S7); high rock/soil concentrations of Ba are present north to Champagne Pool, but not bioavailable to plants. The Ba near Champagne Pool may be present as insoluble salts or mineral precipitates (green dot in Figs. 6-7), halting plant bioavailability. Further away, Ba concentrations in rock/soil samples are low, probably due to samples being organic matter rich.

6.4. Upscaling

With the spread of airborne imaging and now with the new generation satellites, such as PRISMA and EnMAP, a new avenue for chemical monitoring in Earth's surface can emerge. However, both airborne and satellite hyperspectral have some limitations and challenges, data can be impacted by mixed pixels (e.g., background soil, mixed plant species) (Bhatt and Joshi, 2020; Annam and Singla, 2021), nearby highly reflective surfaces (e.g. large areas of silica sinter deposits) (Lyapustin and Kaufman, 2001; Sun et al., 2021), and canopy structure changes (e.

g. canopy height, leaf area) (Almeida et al., 2021; Zhang et al., 2021). In this study, the large pixel size associated with the satellite data resulted in the highest classification accuracies, which is interpreted to be due to spectral mixing and exposure of bare ground (Su, 2016). While these limitations and challenges are inherent of imaging techniques, our workflow returned with highly coherent spatial distributions of element concentrations (Figs. 6-7), matching with independent remote sensing data (TIR and LiDAR), and existing geological/geochemical information.

The current study targeted a New Zealand specific plant species to demonstrate the capability in hyperspectral remote sensing (VNIR/SWIR) to detect slight changes in foliar spectra due to underlying geothermal activity. Similar proxy species in other parts of the world can be studied in geothermal areas, including lichens and shrubs in Italy (*Evernia prunastri, Calluna vulgaris*), sagebrush in USA (*Artemisia tridentata*), shrubs in Kenya (*Tarchonanthus camphoratus*) or grasses in Mexico (*Allenrolfea occidentalis* and *Thypa dominguensis*) (Way and Hall, 2001; Nash et al., 2003; Manzo et al., 2013; Pippucci et al., 2015; González-Acevedo et al., 2018; Lattanzi et al., 2020). These indicator species can provide a global utilisation of hyperspectral remote sensing to track geothermal activity through the foliage.

7. Conclusion

The presented study shows the potential of kanuka foliage as a proxy to map geothermal activity in New Zealand with hyperspectral remote sensing (VNIR/SWIR). This study focused on heat- and metal-induced stress on the physicochemical state of foliage, proposing a new mapping approach using hyperspectral remote sensing. Simultaneously, the height and thermal changes were analysed independently with LiDAR and airborne TIR, showing a positive correlation between temperature increase and plant height reduction in many areas (Fig. 9).

The elements silver (Ag), arsenic (As), barium (Ba), and antimony (Sb) were the focus of this study due to their relevance to understanding and monitoring geothermal areas. Our results confirm that Ag, As and Sb behave similarly in geothermal systems, raising to the surface with deep parental waters and depositing along its pathways at various rates (Bundschuh and Maity, 2015). Soluble forms of these metals can be uptaken by nearby plants and cause stress. High concentrations of Ag, As and Sb in foliage are found near the main focal point where high-chloride near-neutral waters discharge on the surface (i.e. Champagne Pool). Whereas high concentrations of Ba in foliage were found in peripheral areas where cold groundwater mixes with deeper hot fluids (Dunn, 2007) and pH is low (World Health Organization, 2016). To understand the effect of element concentrations in kanuka, we used three spatial scales of remote sensing hyperspectral (VNIR/SWIR) platforms (i.e. laboratory, airborne, and satellite-based). We compared them to elemental concentrations using regression and classification models. Changes in the kanuka foliar spectral response caused by the selected elements in this study were detected in different regions of the electromagnetic spectrum; regions related mainly to chlorophyll absorption, cell structure, and water stress, presenting particular wavelengths for Ba and Sb (Fig. 8).

The presented methodology proved feasible to map element concentration ranges with airborne and satellite-based, with classification model moderate accuracy results between 0.41 and 0.66 (Table 3), congruent spatial map distributions and concordance of results between both dataset results (Fig. 6-7). A similar workflow should be applied and tested for other plant species living in geothermal areas in the future. These results can open new opportunities to explore and monitor geothermal areas with dense plant cover worldwide, with efficient and non-invasive techniques, such as hyperspectral remote sensing.

CRediT authorship contribution statement

Cecilia Rodriguez-Gomez: Conceptualisation, Methodology, Programming, Investigation, Formal analysis, Visualisation, Writing – Original Draft, Writing – Review & Editing.; **Gabor Kereszturi:** Conceptualisation, Methodology, Investigation, Writing – Review & Editing, Supervision, Funding acquisition, Project administration.; **Paramsothy Jeyakumar:** Supervision, Investigation, Writing – Review & Editing.; **Reddy Pullanagari:** Supervision, Investigation, Writing – Review & Editing.; **Robert Reeves:** Supervision, Investigation, Writing – Review & Editing.; Andrew Rae: Supervision, Investigation, Writing – Review & Editing.; **Jonathan Procter:** Supervision.

Declaration of Competing Interest

The authors declare that they have no known competing financial interests or personal relationships that could have appeared to influence the work reported in this paper.

Data availability

Data will be made available on request.

Acknowledgments

Ngati Tahu – Ngati Whaoa Runanga Trustees (40/2015) and the Department of Conservation (78428-GEO) are thanked for supporting our research at Waiotapu and providing field access. School of Agriculture and Environment is acknowledged for providing a PhD scholarship for CRG. This research was founded through the CSG MAU1705 project.

The authors are grateful for the support from Hyperceptions/AeroWorks Ltd for the airborne-based hyperspectral image acquisition, and Specim Ltd. for support on image processing. The thermal infrared imagery was provided by GNS Science. The LiDAR data is available freely from Land Information New Zealand's website (https://www.linz.govt.nz/ data/linz-data-service). The PRISMA hyperspectral satellite-based data was obtained from the PRISMA's website (http://prisma-i.it/index.php/en/).

Supplementary materials

Supplementary material associated with this article can be found, in the online version, at doi:10.1016/j.geothermics.2023.102716.

References

Aitchison, J., 1986. The Statistical Analysis of Compositional Data. Springer, Netherlands. https://doi.org/10.1007/978-94-009-4109-0.

Almeida, D.R.A.de, Broadbent, E.N., Ferreira, M.P., Meli, P., Zambrano, A.M.A., Gorgens, E.B., Resende, A.F., de Almeida, C.T., do Amaral, C.H., Corte, A.P.D., Silva, C.A., Romanelli, J.P., Prata, G.A., de Almeida Papa, D., Stark, S.C., Valbuena, R., Nelson, B.W., Guillemot, J., Féret, J.B., Brancalion, P.H.S, 2021. Monitoring restored tropical forest diversity and structure through UAV-borne hyperspectral and lidar fusion. Rem. Sens. Environ. 264 https://doi.org/10.1016/j.rse.2021.112582. July.

Annam, S., Singla, A., 2021. Spectral unmixing of heavy metal content in agricultural soil using hyperspectral remote sensing data. In: 2021 Sixth International Conference on Image Information Processing (ICIIP), pp. 433–438. https://doi.org/10.1109/ICIIP53038.2021.9702646.

Ballantyne, J.M., Moore, J.N., 1988. Arsenic geochemistry in geothermal systems. Geochim. Cosmochim. Acta 52 (2), 475–483. https://doi.org/10.1016/0016-7037(88)90102-0.

Belgiu, M., Drăgu, L., 2016. Random forest in remote sensing: a review of applications and future directions. ISPRS J. Photogramm. Rem. Sens. 114, 24–31. https://doi.org/10.1016/j.isprsjprs.2016.01.011.

Berrar, D., 2019. Cross-validation. In: Encyclopedia of Bioinformatics and Computational Biology, 1–3. Elsevier, pp. 542–545. https://doi.org/10.1016/B978-0-12-809633-8.20349-X. VolsIssue April.

Bhatt, J.S., Joshi, M.V., 2020. Deep learning in hyperspectral unmixing: a review. In: IGARSS 2020 - 2020 IEEE International Geoscience and Remote Sensing Symposium, pp. 2189–2192. https://doi.org/10.1109/IGARSS39084.2020.9324546.

Bibby, H.M., Glover, R.B., Whiteford, P.C., 1995. The heat output of the Waimangu, Waiotapu-Waikite and Reporoa geothermal systems (NZ): do chloride fluxes provide an accurate measure? In Geotherm. Workshop. https://doi.org/10.2172/895932.
Boothroyd, I.K.G., 2009. Ecological characteristics and management of geothermal systems of the Taupo Volcanic Zone, New Zealand. Geothermics 38 (1), 200–209. https://doi.org/10.1016/j.geothermics.2008.12.010.
Borovička, J., Řanda, Z., Jelínek, E., 2006. Antimony content of macrofungi from clean and polluted areas. Chemosphere 64 (11), 1837–1844. https://doi.org/10.1016/j.chemosphere.2006.01.060.
Bundschuh, J., Maity, J.P., 2015. Geothermal arsenic: occurrence, mobility and environmental implications. Renew. Sustain. Energy Rev. 42, 1214–1222. https://doi.org/10.1016/j.rser.2014.10.092.
Burns, B., 1997. Vegetation change along a geothermal stress gradient at the Te Kopia steamfield. J. R. Soc. N. Z. 27 (2), 279–293. https://doi.org/10.1080/03014223.1997.9517539.
Burns, B., Leathwick, J., 1995. Geothermal Vegetation Dynamics.
Cavallaro, G., Dalla Mura, M., Benediktsson, J.A., Bruzzone, L., 2015. Extended self-dual attribute profiles for the classification of hyperspectral images. IEEE Geosci. Rem. Sens. Lett. 12 (8), 1690–1694. https://doi.org/10.1109/LGRS.2015.2419629.
Chakraborty, R., Kereszturi, G., Pullanagari, R., Durance, P., Ashraf, S., Anderson, C., 2021. Mineral prospecting from biogeochemical and geological information using hyperspectral remote sensing—Feasibility and challenges. J. Geochem. Explor. 232 (15) https://doi.org/10.1016/j.gexplo.2021.106900. March 2021.
Cogliati, S., Sarti, F., Chiarantini, L., Cosi, M., Lorusso, R., Lopinto, E., Miglietta, F., Genesio, L., Guanter, L., Damm, A., Pérez-López, S., Scheffler, D., Tagliabue, G., Panigada, C., Rascher, U., Dowling, T.P.F., Giardino, C., Colombo, R., 2021. The PRISMA imaging spectroscopy mission: overview and first performance analysis. Rem. Sens. Environ. 262, 112499 https://doi.org/10.1016/j.rse.2021.112499. April.
Cox, A., Venkatachalam, P., Sahi, S., Sharma, N., 2016. Silver and titanium dioxide nanoparticle toxicity in plants: a review of current research. Plant Physiol. Biochem. 107, 147–163. https://doi.org/10.1016/j.plaphy.2016.05.022.
Croft, H., Chen, J.M., Zhang, Y., 2014. The applicability of empirical vegetation indices for determining leaf chlorophyll content over different leaf and canopy structures. Ecol. Complexity 17, 119–130. https://doi.org/10.1016/j.ecocom.2013.11.005.
Crowther, T.W., van den Hoogen, J., Wan, J., Mayes, M.A., Keiser, A.D., Mo, L., Averill, C., Maynard, D.S., 2019. The global soil community and its influence on biogeochemistry. Science 365 (6455), eaav0550. https://doi.org/10.1126/science.aav0550.
Curran, P.J., 1989. Remote sensing of foliar chemistry. Rem. Sens. Environ. 30 (3), 271–278. https://doi.org/10.1016/0034-4257(89)90069-2.
Dalponte, M., Ørka, H.O., Gobakken, T., Gianelle, D., Næsset, E., 2013. Tree species classification in boreal forests with hyperspectral data. IEEE Trans. Geosci. Rem. Sens. 51 (5), 2632–2645. https://doi.org/10.1109/TGRS.2012.2216272.
Delalieux, S., Somers, B., Verstraeten, W.W., van Aardt, J.A.N., Keulemans, W., Coppin, P., 2009. Hyperspectral indices to diagnose leaf biotic stress of apple plants, considering leaf phenology. Int. J. Rem. Sens. 30 (8), 1887–1912. https://doi.org/10.1080/01431160802541556.
Dong, T., Liu, J., Shang, J., Qian, B., Ma, B., Kovacs, J.M., Walters, D., Jiao, X., Geng, X., Shi, Y., 2019. Assessment of red-edge vegetation indices for crop leaf area index estimation. Rem. Sens. Environ. 222, 133–143. https://doi.org/10.1016/j.rse.2018.12.032. May 2018.
Duarte, F.J. (1995). Tunable laser applications.
Dunn, C.E. (2007). Biogeochemistry in mineral exploration (M. Hale, Ed.). Elsevier.
Dunn, C.E., Christie, A.B., 2020. Tree ferns and tea trees in biogeochemical exploration for epithermal Au and Ag in New Zealand. Geochem.: Explor., Environ., Anal. 20 (3), 299–314. https://doi.org/10.1144/geochem2019-047.
Farooq, M.A., Islam, F., Ali, B., Najeeb, U., Mao, B., Gill, R.A., Yan, G., Siddique, K.H.M., Zhou, W., 2016. Arsenic toxicity in plants: cellular and molecular mechanisms of its transport and metabolism. Environ. Exp. Bot. 132, 42–52. https://doi.org/10.1016/j.envexpbot.2016.08.004.
Feng, R., Wei, C., Tu, S., Ding, Y., Wang, R., Guo, J., 2013. The uptake and detoxification of antimony by plants: a review. Environ. Exp. Bot. 96, 28–34. https://doi.org/10.1016/j.envexpbot.2013.08.006.
Finnegan, P.M., Chen, W., 2012. Arsenic toxicity: the effects on plant metabolism. Front. Physiol. 3, 1–18. https://doi.org/10.3389/fphys.2012.00182. *JUN*(June).
Ghamisi, P., Plaza, J., Chen, Y., Li, J., Plaza, A.J., 2017. Advanced spectral classifiers for hyperspectral images: a review. IEEE Geosci. Rem. Sens. Mag. 5 (1), 8–32. https://doi.org/10.1109/MGRS.2016.2616418.
Ghosh, A., Joshi, P.K., 2014. A comparison of selected classification algorithms for mappingbamboo patches in lower Gangetic plains using very high resolution WorldView 2 imagery. Int. J. Appl. Earth Observ. Geoinf. 26 (1), 298–311. https://doi.org/10.1016/j.jag.2013.08.011.
Giggenbach, W., Sheppard, D.S., Robinson, B.W., Stewart, M.K., Lyon, G.L., 1994. Geochemical structure and position of the Waiotapu geothermal field, New Zealand. Geothermics 23 (5–6), 599–644. https://doi.org/10.1016/0375-6505(94)90022-1.
Given, D.R., 1980. Vegetation on heated soils at Karapiti, Central North Island, New Zealand, And its relation to ground. N.Z. J. Bot. 18 (1), 1–13. https://doi.org/10.1080/0028825X.1980.10427227.
González-Acevedo, Z.I., García-Zarate, M.A., Núñez-Zarco, E.A., Anda-Martín, B.I., 2018. Heavy metal sources and anthropogenic enrichment in the environment around the Cerro Prieto Geothermal Field, Mexico. Geothermics 72 (May 2017), 170–181. https://doi.org/10.1016/j.geothermics.2017.11.004.
Götze, C., Jung, A., Merbach, I., Wennrich, R., Gläßer, C., 2010. Spectrometric analyses in comparison to the physiological condition of heavy metal stressed floodplain vegetation in a standardised experiment. Central Eur. J. Geosci. 2 (2), 132–137. https://doi.org/10.2478/v10085-010-0002-y.
Grange, L., 1937. The Geology of the Rotorua-Taupo Subdivision, Rotorua and Kaimanawa Divisions, 37. New Zealand Department of Scientific and Industrial Research Bulletin., pp. 86–105
Grindley, G., Mumme, T., Kohn, B., 1994. Stratigraphy, paleomagnetism, geochronology and structure of silicic volcanic rocks, Waiotapu/Paeroa range area, New Zealand. Geothermics 23 (5–6), 473–499. https://doi.org/10.1016/0375-6505(94)90014-0.
Hadfield, J., Nicole, D., Rosen, M., Wilson, C.J.L., Morgenstern, U., 2001. Hydrogeology of Lake Taupo catchment: phase 1. Environ. Waikato Techn. Rep. *2001/01*.
Hedenquist, J.W., 1982. Fluid flow in the Waiotapu geothermal system, New Zealand: implications for its potential. In: Proceedings of the New Zealand Geothermal Workshop, pp. 61–67.
Hedenquist, J.W., 1991. Boiling and dilution in the shallow portion of the Waiotapu geothermal system, New Zealand. Geochim. Cosmochim. Acta 55 (10), 2753–2765. https://doi.org/10.1016/0016-7037(91)90442-8.
Hedenquist, J.W., Browne, P.R.L., 1989. The evolution of the Waiotapu geothermal system, New Zealand, based on the chemical and isotopic composition of its fluids, minerals and rocks. Geochim. Cosmochim. Acta 53 (9), 2235–2257. https://doi.org/10.1016/0016-7037(89)90347-5.
Hedenquist, J.W., Henley, R.W., 1985. Hydrothermal eruptions in the Waiotapu geothermal system, New Zealand; their origin, associated breccias, and relation to precious metal mineralization. Econ. Geol. 80 (6), 1640–1668. https://doi.org/10.2113/gsecongeo.80.6.1640.
Hong, H., Xiaoling, G., Hua, Y., 2016a. Variable selection using mean decrease accuracy and mean decrease gini based on random forest. In: 2016 7th IEEE International Conference on Software Engineering and Service Science (ICSESS), pp. 219–224. https://doi.org/10.1109/ICSESS.2016.7883053.
Hong, H., Xiaoling, G., Hua, Y., 2016b. Variable selection using mean decrease accuracy and mean decrease gini based on random forest. In: 2016 7th IEEE International Conference on Software Engineering and Service Science (ICSESS), pp. 219–224. https://doi.org/10.1109/ICSESS.2016.7883053.
Hood, S.B., Cracknell, M.J., Gazley, M.F., Reading, A.M., 2019. Element mobility and spatial zonation associated with the Archean Hamlet orogenic Au deposit, Western Australia: implications for fluid pathways in shear zones. Chem. Geol. 514 (December 2018), 10–26. https://doi.org/10.1016/j.chemgeo.2019.03.022.
Hunt, T.M., Glover, R.B., Wood, C.P., 1994. Waimangu, Waiotapu, and Waikite geothermal systems, New Zealand: background and history. Geothermics 23 (5–6), 379–400. https://doi.org/10.1016/0375-6505(94)90010-8.
Kabata-Pendias, A., 2010. Trace Elements in Soils and Plants. Angew. Chem. Int. Ed. 6 (11), 951–952. https://doi.org/10.1201/b10158.
Kaya, E., Hochstein, M.P., Yeh, A., Sullivan, M.J.O., 2015. Aspects of natural heat transfer of a geothermal system in moderate terrain: the greater Waiotapu geothermal system, New Zealand. In: *Proceedings World Geothermal Congress 2015, April*, pp. 1–12.
Kaya, E., O'Sullivan, M.J., Hochstein, M.P., 2014. A three dimensional numerical model of the Waiotapu, Waikite and Reporoa geothermal areas, New Zealand. J. Volcanol. Geotherm. Res. 283, 127–142. https://doi.org/10.1016/j.jvolgeores.2014.07.008.
Khan, A., Khan, S., Khan, M.A., Qamar, Z., Waqas, M., 2015. The uptake and bioaccumulation of heavy metals by food plants, their effects on plants nutrients, and associated health risk: a review. Environ. Sci. Pollut. Res. 22 (18), 13772–13799. https://doi.org/10.1007/s11356-015-4881-0.
Kissling, W.M., Weir, G.J., 2005. The spatial distribution of the geothermal fields in the Taupo Volcanic Zone, New Zealand. J. Volcanol. Geotherm. Res. 145 (1–2), 136–150. https://doi.org/10.1016/j.jvolgeores.2005.01.006.
Kokaly, R.F., Skidmore, A.K., 2015. Plant phenolics and absorption features in vegetation reflectance spectra near 1.66μm. Int. J. Appl. Earth Observ. Geoinf. 43, 55–83. https://doi.org/10.1016/j.jag.2015.01.010.
Lattanzi, P., Benesperi, R., Morelli, G., Rimondi, V., Ruggieri, G., 2020. Biomonitoring studies in geothermal areas: a review. Front. Environ. Sci. 8 (x), 1–7. https://doi.org/10.3389/fenvs.2020.579343.
Li, J., Sun, Y., Jiang, X., Chen, B., Zhang, X., 2018. Arbuscular mycorrhizal fungi alleviate arsenic toxicity to Medicago sativa by influencing arsenic speciation and partitioning. Ecotoxicol. Environ. Saf. 157 (18), 235–243. https://doi.org/10.1016/j.ecoenv.2018.03.073.
Lloyd, E.F., 1959. The Hot Springs and Hydrothermal Eruptions of Waiotapu. New Zealand J. Geol. Geophys. 2 (1), 141–176. https://doi.org/10.1080/00288306.1959.10431319.
Lyapustin, A.I., Kaufman, Y.J., 2001. Role of adjacency effect in the remote sensing of aerosol. J. Geophys. Res.: Atmos. 106 (D11), 11909–11916. https://doi.org/10.1029/2000JD900647.
Macur, R.E., Langner, H.W., Kocar, B.D., Inskeep, W.P., 2004. Linking geochemical processes with microbial community analysis: successional dynamics in an arsenic-rich, acid-sulphate-chloride geothermal spring. Geobiology 2 (3), 163–177. https://doi.org/10.1111/j.1472-4677.2004.00032.x.
Manzo, C., Salvini, R., Guastaldi, E., Nicolardi, V., Protano, G., 2013. Reflectance spectral analyses for the assessment of environmental pollution in the geothermal site of Mt. Amiata (Italy). Atmos. Environ. 79, 650–665. https://doi.org/10.1016/j.atmosenv.2013.06.038.
McKinley, J.M., Hron, K., Grunsky, E.C., Reimann, C., de Caritat, P., Filzmoser, P., van den Boogaart, K.G., Tolosana-Delgado, R., 2016. The single component geochemical map: fact or fiction? J. Geochem. Explor. 162, 16–28. https://doi.org/10.1016/j.gexplo.2015.12.005.
Mia, M.B., Bromley, C.J., Fujimitsu, Y., 2012. Monitoring heat flux using Landsat TM/ETM+ thermal infrared data—a case study at Karapiti ('Craters of the Moon') thermal area, New Zealand. J. Volcanol. Geotherm. Res. 235–236, 1–10. https://doi.org/10.1016/j.jvolgeores.2012.05.005.

Milicich, S.D., Mortimer, N., Villamor, P., Wilson, C.J.N., Sagar, M.W., Ireland, T.R., Milicich, S.D., Mortimer, N., Villamor, P., Wilson, C.J.N., Chambefort, I., Sagar, M. W., Ireland, T.R., Mesozoic, T., 2020. The Mesozoic terrane boundary beneath the Taupo Volcanic Zone, New Zealand, and potential controls on geothermal system characteristics The Mesozoic terrane boundary beneath the Taupo Volcanic Zone, New. New Zealand J. Geol. Geophys. 0 (0), 1–12. https://doi.org/10.1080/00288306.2020.1823434.

Molinaro, A.M., Simon, R., Pfeiffer, R.M., 2005. Prediction error estimation: a comparison of resampling methods. Bioinformatics 21 (15), 3301–3307. https://doi.org/10.1093/bioinformatics/bti499.

Mongillo, M.A., 1994. Aerial thermal infrared mapping of the Waimangu-Waiotapu geothermal region, New Zealand. Geothermics 23 (5–6), 511–526. https://doi.org/10.1016/0375-6505(94)90016-7.

Moyersoen, B., Beever, R.E., 2004. Abundance and characteristics of Pisolithus ectomycorrhizas in New Zealand geothermal areas. Mycologia 96 (6), 1225–1232. https://doi.org/10.1080/15572536.2005.11832871.

Muriithi, F.K., 2015. Centered log-ratio (clr) transformation and robust principal component analysis of long-term NDVI data reveal vegetation activity linked to climate processes. Climate 3 (1), 135–149. https://doi.org/10.3390/cli3010135.

Muukkonen, P., 2005. Vegetation of geothermal areas on the North Island, New Zealand. Terra 117 (4), 265–278.

Nairn, I.A., Wood, C.P., Bailey, R.A., 1994. The Reporoa Caldera, Taupo Volcanic Zone: source of the Kaingaroa Ignimbrites. Bull. Volcanol. 56 (6–7), 529–537. https://doi.org/10.1007/BF00302833.

Nash, G.D., Moore, J.N., Sperry, T., 2003. Vegetal-spectral anomaly detection at the Cove Fort-Sulphurdale thermal anomaly, Utah, USA: implications for use in geothermal exploration. Geothermics 32 (2), 109–130. https://doi.org/10.1016/S0375-6505(03)00012-9.

Pippucci, A., Lorenzi, R., Spanò, C., Sorce, C., 2015. Stress-induced changes to the flora in a geothermal field in central Italy. Acta Physiol. Plantarum (10), 37. https://doi.org/10.1007/s11738-015-1953-1.

Pirajno, F., 2009. Hydrothermal Processes and Mineral Systems. J. Chem. Inf Model 53 (9). https://doi.org/10.1007/978-1-4020-8613-7. Springer Netherlands.

Poblete, T., Camino, C., Beck, P.S.A., Hornero, A., Kattenborn, T., Saponari, M., Boscia, D., Navas-Cortes, J.A., Zarco-Tejada, P.J., 2020. Detection of Xylella fastidiosa infection symptoms with airborne multispectral and thermal imagery: assessing bandset reduction performance from hyperspectral analysis. ISPRS J. Photogramm. Rem. Sens. 162 (October 2019), 27–40. https://doi.org/10.1016/j.isprsjprs.2020.02.010.

Pullanagari, R.R., Kereszturi, G., Yule, I.J., 2016. Mapping of macro and micro nutrients of mixed pastures using airborne AisaFENIX hyperspectral imagery. ISPRS J. Photogramm. Rem. Sens. 117, 1–10. https://doi.org/10.1016/j.isprsjprs.2016.03.010.

Rathod, P.H., Brackhage, C., Müller, I., Van der Meer, F.D., Noomen, M.F., 2018. Assessing metal-induced changes in the visible and near-infrared spectral reflectance of leaves: a pot study with sunflower (Helianthus annuus L.). J. Indian Soc. Rem. Sens. 3 (3) https://doi.org/10.1007/s12524-018-0846-3.

Reeves, R., & Sanders, F. (2019). 2019 thermal infrared survey of the Waiotapu geothermal field. August. https://doi.org/10.21420/ZD6D-GD88.

Reich, M., Román, N., Barra, F., Morata, D., 2020. Silver-rich chalcopyrite from the active Cerro Pabellón geothermal system, Northern Chile. Minerals 10 (2), 113. https://doi.org/10.3390/min10020113.

Richter, R., 1998. Correction of satellite imagery over mountainous terrain. Appl. Opt. 37 (18), 4004. https://doi.org/10.1364/AO.37.004004.

Rodriguez-Gomez, C., Kereszturi, G., Reeves, R., Rae, A., Pullanagari, R., Jeyakumar, P., Procter, J.N., 2021. Lithological mapping of Waiotapu Geothermal Field (New Zealand) using hyperspectral and thermal remote sensing and ground exploration techniques. Geothermics 96 (June), 102195. https://doi.org/10.1016/j.geothermics.2021.102195.

Rosipal, R., 2003. Kernel partial least squares for nonlinear regression and discrimination. Neural Netw. World 13 (3), 291–300.

Rowland, J.V., Sibson, R.H., 2004. Structural controls on hydrothermal flow in a segmented rift system, Taupo Volcanic Zone, New Zealand. Geofluids 4 (4), 259–283. https://doi.org/10.1111/j.1468-8123.2004.00091.x.

Rowland, J.V., Simmons, S.F., 2012. Hydrologic, magmatic, and tectonic controls on hydrothermal flow, Taupo Volcanic Zone, New Zealand: implications for the formation of epithermal vein deposits. Econ. Geol. 107 (3), 427–457. https://doi.org/10.2113/econgeo.107.3.427.

Roy, P.S., 1989. Spectral reflectance characteristics of vegetation and their use in estimating productive potential. Proc.: Plant Sci. 99 (1), 59–81. https://doi.org/10.1007/BF03053419.

Sanches, I.D., Souza Filho, C.R., Magalhães, L.A., Quitério, G.C.M., Alves, M.N., Oliveira, W.J., 2013a. Unravelling remote sensing signatures of plants contaminated with gasoline and diesel: an approach using the red edge spectral feature. Environ. Pollut. 174, 16–27. https://doi.org/10.1016/j.envpol.2012.10.029.

Sanches, I.D., Souza Filho, C.R., Magalhães, L.A., Quitério, G.C.M., Alves, M.N., Oliveira, W.J., 2013b. Unravelling remote sensing signatures of plants contaminated with gasoline and diesel: an approach using the red edge spectral feature. Environ. Pollut. 174, 16–27. https://doi.org/10.1016/j.envpol.2012.10.029.

Savitzky, A., Golay, M.J.E., 1964. Smoothing and differentiation of data by simplified least squares procedures. Anal. Chem. 36 (8), 1627–1639. https://doi.org/10.1021/ac60214a047.

Schläpfer, D., Richter, R., 2002. Geo-atmospheric processing of airborne imaging spectrometry data. Part 1: parametric orthorectification. Int. J. Rem. Sens. 23 (13), 2609–2630. https://doi.org/10.1080/01431160110115825.

Seebeck, H., Nicol, A., Villamor, P., Ristau, J., Pettinga, J., 2014. Structure and kinematics of the Taupo Rift, New Zealand. Tectonics 33 (6), 1178–1199. https://doi.org/10.1002/2014TC003569.

Shahid, M., Dumat, C., Khalid, S., Schreck, E., Xiong, T., Niazi, N.K., 2017. Foliar heavy metal uptake, toxicity and detoxification in plants: a comparison of foliar and root metal uptake. J. Hazard. Mater. 325, 36–58. https://doi.org/10.1016/j.jhazmat.2016.11.063.

Shtangeeva, I., Bali, R., Harris, A., 2011. Bioavailability and toxicity of antimony. J Geochem Explor 110 (1), 40–45. https://doi.org/10.1016/j.gexplo.2010.07.003.

Simmons, S.F., Brown, K.L., Browne, P.R.L., Rowland, J.V., 2016a. Gold and silver resources in Taupo Volcanic Zone geothermal systems. Geothermics 59, 205–214. https://doi.org/10.1016/j.geothermics.2015.07.009.

Simmons, S.F., Brown, K.L., Browne, P.R.L., Rowland, J.V., 2016b. Gold and silver resources in Taupo Volcanic Zone geothermal systems. Geothermics 59, 205–214. https://doi.org/10.1016/j.geothermics.2015.07.009.

Sims, D.A., Gamon, J.A., 2002. Relationships between leaf pigment content and spectral reflectance across a wide range of species, leaf structures and developmental stages. Rem. Sens Environ. 81 (2–3), 337–354. https://doi.org/10.1016/S0034-4257(02)00010-X.

Sleimi, N., Kouki, R., Hadj Ammar, M., Ferreira, R., Pérez-Clemente, R., 2021. Barium effect on germination, plant growth, and antioxidant enzymes in Cucumis sativus L. plants. Food Sci. Nutr. 9 (4), 2086–2094. https://doi.org/10.1002/fsn3.2177.

Slonecker, T., Haack, B., Price, S., 2009. Spectroscopic analysis of arsenic uptake in Pteris ferns. Rem. Sens. (Basel) 1 (4), 644–675. https://doi.org/10.3390/rs1040644.

Smale, M.C., Wiser, S.K., Bergin, M.J., Fitzgerald, N.B., 2018. A classification of the geothermal vegetation of the Taupō Volcanic Zone, New Zealand. J. R. Soc. N. Z. 48 (1), 21–38. https://doi.org/10.1080/03036758.2017.1322619.

Smith, C.L., Ficklin, W.H., Thompson, J.M., 1987. Concentrations of arsenic, antimony, and boron in steam and steam condensate at The Geysers, California. J. Volcanol. Geotherm. Res. 32 (4), 329–341. https://doi.org/10.1016/0377-0273(87)90083-7.

Steiner, A., 1963. The rocks penetrated by drillholes in the Waiotapu thermal area, and their hydrothermal alteration. In: Waiotapu Geothermal Field, 155. New Zealand Department of Scientific and Industrial Research Bulletin., pp. 26–35

Su, T.C., 2016. A filter-based post-processing technique for improving homogeneity of pixel-wise classification data. Eur. J. Rem. Sens. 49, 531–552. https://doi.org/10.5721/EuJRS20164928.

Sun, B., Schafer, M., Ehrlich, A., Jakel, E., Wendisch, M., 2021. Influence of atmospheric adjacency effect on top-of-atmosphere radiances and its correction in the retrieval of Lambertian surface reflectivity based on three-dimensional radiative transfer. Rem. Sens. Environ. 263 (May) https://doi.org/10.1016/j.rse.2021.112543.

Suwa, R., Jayachandran, K., Nguyen, N.T., Boulenouar, A., Fujita, K., Saneoka, H., 2008. Barium toxicity effects in soybean plants. Arch. Environ. Contam. Toxicol. 55 (3), 397–403. https://doi.org/10.1007/s00244-008-9132-7.

Tschan, M., Robinson, B.H., Schulin, R., 2009. Antimony in the soil—plant system—a review. Environ. Chem. 6 (2), 106–115. https://doi.org/10.1071/EN08111.

Tucker, C.J., 1979. Remote sensing of leaf water content in the near infrared. Rem. Sens. Environ. 10, 23–32.

Ubeynarayana, N., Jeyakumar, P., Bishop, P., Pereira, R.C., Anderson, C.W.N., 2021. Effect of soil cadmium on root organic acid secretion by forage crops. Environ. Pollut. 268, 115839 https://doi.org/10.1016/j.envpol.2020.115839.

van der Linden, S., Rabe, A., Held, M., Jakimow, B., Leitão, P., Okujeni, A., Schwieder, M., Suess, S., Hostert, P., 2015. The EnMAP-Box—a toolbox and application programming interface for EnMAP data processing. Rem. Sens. (Basel) 7 (9), 11249–11266. https://doi.org/10.3390/rs70911249.

Van Manen, S.M., Reeves, R., 2012a. An assessment of changes in kunzea ericoides var. Microflora and other hydrothermal vegetation at the Wairakei-Tauhara geothermal field, New Zealand. Environ. Manag. 50 (4), 766–786. https://doi.org/10.1007/s00267-012-9899-1.

Van Manen, S.M., Reeves, R., 2012b. An assessment of changes in kunzea ericoides var. Microflora and other hydrothermal vegetation at the Wairakei-Tauhara geothermal field, New Zealand. Environ. Manag. 50 (4), 766–786. https://doi.org/10.1007/s00267-012-9899-1.

Wallace, A., Mueller, R.T., Wood, R.A., 1980. Arsenic phytotoxicity and interactions in bush bean plants grown in solution culture. J. Plant Nutr. 2 (1–2), 111–113. https://doi.org/10.1080/01904168009362747.

Wang, F., Gao, J., Zha, Y., 2018. Hyperspectral sensing of heavy metals in soil and vegetation: feasibility and challenges. ISPRS J. Photogramm. Rem. Sens. 136, 73–84. https://doi.org/10.1016/j.isprsjprs.2017.12.003.

Wang, P., Lombi, E., Sun, S., Scheckel, K.G., Malysheva, A., McKenna, B.A., Menzies, N. W., Zhao, F.J., Kopittke, P.M., 2017. Characterizing the uptake, accumulation and toxicity of silver sulfide nanoparticles in plants. Environ. Sci.: Nano 4 (2), 448–460. https://doi.org/10.1039/c6en00489j.

Waskom, M., 2021. Seaborn: statistical data visualization. J. Open Source Softw. 6 (60), 3021. https://doi.org/10.21105/joss.03021.

Way, W., Hall, S., 2001. Cost-effective vegetation anomaly mapping for geotherma exploration. In: PROCEEDINGS: Twenty-Sixth Workshop on. Geothermal Reservoir Engineering Stanford University, Stanford, California. *January 29-30, 2001 SGP-TR-1682*.

Weissberg, B.G., 1969. Gold-silver ore-grade precipitates from new zealand thermal waters. Econ. Geol. 64, 95–108.

Wilson, C.J.N., Houghton, B.F., McWilliams, M.O., Lanphere, M.A., Weaver, S.D., Briggs, R.M., 1995. Volcanic and structural evolution of Taupo Volcanic Zone, New Zealand: a review. J. Volcanol. Geotherm. Res. 68 (1–3), 1–28. https://doi.org/10.1016/0377-0273(95)00006-G.

Wilson, N., Webster-Brown, J., Brown, K., 2012. The behaviour of antimony released from surface geothermal features in New Zealand. J. Volcanol. Geotherm. Res. 247–248, 158–167. https://doi.org/10.1016/j.jvolgeores.2012.08.009.

Wilson, S.C., Lockwood, P.V., Ashley, P.M., Tighe, M., 2010. The chemistry and behaviour of antimony in the soil environment with comparisons to arsenic: a critical review. Environ. Pollut. 158 (5), 1169–1181. https://doi.org/10.1016/j.envpol.2009.10.045.

Wold, S., Sjöström, M., Eriksson, L., 2001. PLS-regression: a basic tool of chemometrics. Chemometr. Intell. Lab. Syst. 58 (2), 109–130. https://doi.org/10.1016/S0169-7439(01)00155-1.

Wood, C.P., 1994a. Aspects of the geology of Waimangu, Waiotapu, Waikite and Reporoa geothermal systems, Taupo Volcanic Zone, New Zealand. Geothermics 23 (5–6), 401–421. https://doi.org/10.1016/0375-6505(94)90011-6.

Wood, C.P., 1994b. Aspects of the geology of Waimangu, Waiotapu, Waikite and Reporoa geothermal systems, Taupo Volcanic Zone, New Zealand. Geothermics 23 (5–6), 401–421. https://doi.org/10.1016/0375-6505(94)90011-6.

World Health Organization, W. H. O. (2016). *Barium in Drinking-Water.*.

Xia, X., Li, X., Wang, C., Liu, X., Liu, M., 2014. A hyperspectral index sensitive to subtle changes in the canopy chlorophyll content under arsenic stress. Int. J. Appl. Earth Observ. Geoinf. 36, 41–53. https://doi.org/10.1016/j.jag.2014.10.017.

Zeng, Y., Chen, M., Hao, D., Damm, A., Badgley, G., Rascher, U., Johnson, J.E., Dechant, B., Siegmann, B., Ryu, Y., Qiu, H., Krieger, V., Panigada, C., Celesti, M., Miglietta, F., Yang, X., Berry, J.A., 2022. Combining near-infrared radiance of vegetation and fluorescence spectroscopy to detect effects of abiotic changes and stresses. Rem. Sens. Environ. 270 (December 2021), 112856 https://doi.org/10.1016/j.rse.2021.112856.

Zhang, Y., Hui, J., Qin, Q., Sun, Y., Zhang, T., Sun, H., Li, M., 2021. Transfer-learning-based approach for leaf chlorophyll content estimation of winter wheat from hyperspectral data. Rem. Sens. Environ. 267 (July), 112724 https://doi.org/10.1016/j.rse.2021.112724.